EUMETSAT
OSI SAF
OCEAN AND SEA ICE

Coastal PenWP

OSI_VS21_03

Authors: **G. Grieco**[1], M. Portabella[2], J. Vogelzang[3], A. Verhoef[3], A. Stoffelen[3]

[1] Institute of Marine Sciences (ISMAR-CNR)

[2] Barcelona Expert Center (BEC ICM-CSIC)

[3] Koninklijk Nederlands Meteorologisch Instituut (KNMI)

Visiting Scientist Activity

Technical Report

Date: 31 March 2022

Contents

Abstract

This study presents a refinement of the assessment of QuikSCAT normalized radar cross sections (σ_0s) noise, together with an assessment of the intra-egg biases induced by the incidence angle variation and their impact on noise estimates. In addition, it describes a new implementation of Land Contribution Radio (LCR). Furthermore, it shows the implementation of an LCR-based σ_0 correction scheme to reduce the impact of land contaminations. Finally, corrected σ_0s are integrated in the four pol-view σ_0s to be used in the retrieval step. Four different averaging methodologies are considered, which differentiate according to the weight assigned to each slice: homogeneous (boxcar),

K_p dependent, lcr dependent, or Gaussian dependent on the retrieval error. The results confirm that the noise levels provided in the full resolution files have some significant differences with the estimates. In particular, external H-Pol acquisitions are noisier than expected, especially those closer to the antenna for medium-high wind regimes, while inner acquisitions are less noisy than reported in the files, especially those V-Pol. The impact of the intra-egg biases on the noise estimates is less than 7%, therefore all previous conclusions are valid.

The correction of σ_0s shows that the new LCR method (LCR^{full}) seems to provide more suitable estimates of LCR. The correction method is effective in reducing the coastal σ_0 values, even if many negative values occur. This trend is expected and the main reason is due to the high σ_0-dependent noise level that affects QuikSCAT measurements. A new formulation of the correction scheme that considers an additional noise-dependent regularization parameter is recommended. Finally, integration methodologies show some differences, but all show some residual contamination near the shore. These preliminary results are not sufficient to select the most suitable one. It is recommended to make this choice after the retrieval step is performed. The software structure is robust, but the LCR computation is very time-consuming. An optimization of the code is required after it is implemented in a suitable low-level programming language.

1 Introduction

Coastal wind monitoring is a fundamental asset for several scientific and civil applications. In fact, accurate coastal winds are strategic both for weather and ocean forecasting, as well as for climate monitoring. Furthermore, they play a key role in the dispersion of air pollutants and greatly affect marine currents and the local microclimate. Finally, the industry of wind-derived energy production also is looking at this geophysical parameter with great interest. All of these aspects affect the lives of many million people living on the seaside, which represents the majority of the world population. Since the launch of Seasat in June 1978, scatterometer-derived winds have rapidly become the gold standard for ocean wind field monitoring. Today, its accuracy is within ≈ 1 ms^{-1} in speed and $\approx \pm 20^o$ in direction. However, the quality of coastal winds may be poorer due to land contamination, with a consequent reduction in both sampling and accuracy. Therefore, some ad hoc preprocessing of normalized radar cross section (σ_0) measurements is needed to mitigate such effects and consequently improve both aspects. The authors of [1] show how to properly quantify the land contamination of QuikSCAT slices by introducing the land contribution ratio (LCR) index. They show how to improve both sampling and accuracy by discarding only excessively contaminated footprints. A similar approach is also applied to ASCAT measurements by the authors of [2], after the spatial response function (SRF) of the instrument has been properly modeled [3]. The authors of [4] show how to correct the contaminated σ_0 with an LCR-based correction scheme. In this way, the number of σ_0s discarded is considerably reduced. The authors of [5] show the implementation of the QuikSCAT SRF by following the analytical indications given in [1]. In addition, they compare this model with the one derived from a look-up table of precomputed parameterized SRFs, provided by the group of Prof. Dave Long from the Brigham Young University. The results show that some non-negligible differences are apparent, suggesting that their impact on the retrieved winds could be relevant.

Noise characterization is fundamental to correctly approach the inverse problem [6]. The authors of [7] show how to estimate the noise-to-signal ratio of σ_0 (K_p) for ASCAT measurements. In [8], the authors show how to estimate K_p and compare the results with the median values provided in QuikSCAT full resolution level 1B (FR L1B) files. The results of [8] show that the differences may be large, especially for the peripheral slices of the horizontally polarized (H-pol) acquisitions. The estimated K_ps ($\hat{K}_p$s) have been validated against a theoretical model derived from [9], suggesting that the detected differences are real. In addition, the variation of the angle of incidence *intra* egg causes some biases that should be taken into account in the retrieval. The

works [5] and [8] have been carried out in the frame of an OSI-SAF project aimed at providing users with a QuikSCAT-derived wind data set spanning the entire mission. In this study, we present a refined evaluation of $\hat{K}_p$, together with the evaluation of the impact of intra-egg biases induced by the incidence angle on $\hat{K}_p$. In addition, a refined assessment of the LCR index is presented, and an LCR-based σ_0 correction scheme is applied. Finally, we present an evaluation of several averaging procedures for the integrated σ_0 quadruplets. This document is organized as follows: Section 2 describes the software architecture; Section 3 describes the QuikSCAT dataset used in this study; Section 4 describes the methodology used to refine the evaluation of $\hat{K}_p$, to assess the impact of the incidence angle-induced biases on $\hat{K}_p$, the new way to calculate the LCR index, the LCR-based σ_0 correction scheme and the integration procedures to calculate the σ_0 quadruplets needed for the retrievals; Section 5 reports on the results; Section 6 shows the conclusions and section 7 gives some ideas for future developments.

2 Description of the software

The entire software used in this study is based on the Pencil Beam Wind Processor `PenWP`, written mainly in Fortran 90 with some parts written in C for handling data from the SeaWinds (on QuikSCAT or ADEOS-II), OSCAT (on Oceansat-2), HSCAT (on HY-2A) and RapidScat (on the International Space Station) scatterometer instruments. `PenWP` is an operational software package developed by the EUMETSAT Ocean and Sea Ice Satellite Application Facility (OSI SAF, `https://osi-saf.eumetsat.int`) and freely distributed upon request at the NWP-SAF website `https://nwp-saf.eumetsat.int/site/software/scatterometer/download/`. The flow chart of `PenWP` for QuikSCAT FR files is represented by the black framed blocks on the left side of the figure 1. `PenWP` can only handle pre-processed QuikSCAT bufr files, which are obtained by means of the tool `seawinds_l1b_bufr`, provided in the suite. This tool integrates the L1B slice σ_0s into quadruplets, which are then stored in the bufr file. At the moment, `PenWP` can only produce QuikSCAT 25 km output wind grids. The code needs to be updated to provide finer output grids. This is left for future developments.

The idea is to keep `PenWP` as is and supply it with modified QuikSCAT FR L1B files. These files are identical to the original ones but for the fields `slice_sigma0` and `slice_qual_flag`. These fields contain the corrected σ_0 values and the updated quality flags, respectively.

Four additional patches have been created to produce the modified QuikSCAT FR L1B files. They are reported in figure 1 in different colors. The modified QuikSCAT FR L1B files are output by the block σ_0 `correction` in figure 1. This procedure requires several input files, namely the original QuikSCAT FR L1B file (the red framed block `QS FR` in figure 1), a file containing the distance of the output wind vector cells (WVCs) from the shoreline (the light blue block `d2c_L2B`), a file containing the slice LCR (the green block `LCR L1B`), and a file containing the map of the slice indices into the output WVC grid indices (the orange block `slice 2 wvc`).

The file `d2c_L2B` is output by the block `distance_to_coast`, together with the file `d2c_L1B`. This procedure computes the distance from the shoreline with a precision of 1 km. More information about this tool can be found in [4]. Both distance files are used to reduce the computational burden. In fact, the LCR computation is limited only to the slices whose centroids are within $\pm$ 50 km from the coast, as there is no reason to expect that the farther slices may have an index different from 0 or 1. Even using this strategy, the CPU user time needed to compute LCR for the orbit with ID 40653 is 55.4 hours. It is important to note that even if we are only interested in sea WVCs, the procedure σ_0 `correction` involves slices with LCR values in the
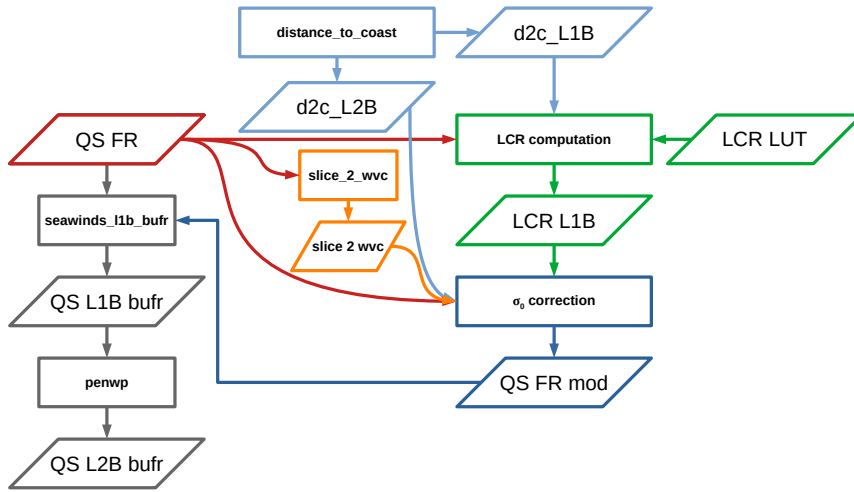
Figure 1: Software flow chart

interval $[0, 1]$, to improve the fit of the regression parameters. Slices with LCR $\approx > 0.5$ are usually internal. Furthermore, no regressions are necessary for WVCs farther than 100 km from the coast.

Block `LCR computation` calculates the LCR. It needs three input files, namely the original QuikSCAT FR L1B file, the file containing the distance of the slice centroids from the shoreline, and the LUT of the parameterized precomputed SRFs. Finally, the procedure `slice_2_wvc` (orange framed block) maps the slice indices into the WVCs indices.

All patches are written in Python. They are planned to be rewritten in FORTRAN 90 and integrated into the package `PenWP` with the aim of improving their efficiency and code handling. This is left for the future.

3 Dataset

In this study, a data set of 14 orbits, each corresponding to a QuikSCAT FR L1B file, has been used. They represent all files that were acquired during the 10th of April 2007, marked with orbit IDs 40651 to 40664. QuikSCAT FR L1B files can be freely downloaded from the PODAAC web site [10]. The full content of these files is well described in the QuikSCAT reference manual [11]. Here after, only the relevant information for this study is reported. The fields used in this study are listed in the table 1. The acronyms "sc", "ECEF" stand for "spacecraft" and "Earth-Centered Earth-Fixed", respectively. All arrays are provided in a time-ordered fashion. `n_f`, `n_p`, and `n_s`, stand for "number of frames", "number of pulses", and "number of slices", respectively. `n_p` is equal to 100 and `n_s` to 8, while `n_f` may vary with the orbit. Its typical value is around 11240. All data have been Quality Controlled (QCed) according to the following scheme:

- `frame_err_status` is required to be 0. This requirement ensures that neither an unusual instrument condition applies, nor bad ephemeris, nor bad attitude.

- bit 4 (0-based) of `frame_qual_flag` is required to be 0, otherwise bad data are present in the frame.

- bits 0-3 of `frame_inst_status` are required to be 0, while bits 4-6 are required to be "011".

- bits 0, 3-9 of `sigma0_qual_flag` are required to be 0. This condition ensures that

    - The egg is usable (bit 0)
    - The egg σ_0 is in an acceptable range (bit 3) (not required for noise estimation)
    - The scatterometer pulse is acceptable (bit 4)
    - The σ_0 cell location algorithm converges (bit 5)
    - The frequency shift is within the range of the x factor table (bit 6)
    - The spacecraft temperature is within the calibration coefficient range (bit 7)
    - An applicable attitude record was found for this σ_0 (bit 8)
    - Interpolated ephemeris data are acceptable for this σ_0 (bit 9)

Bits 1, 2, and 3 account for the SNR level, the sign of σ_0, and the admitted range of σ_0s. No constraint is applied to them for the noise estimation of the slice σ_0. In fact, a fair estimate of the noise of the slice σ_0 must take into account both low SNR measurements, negative values, and σ_0s outside of the expected range; otherwise, the distribution of σ_0 could be truncated and some artificial biases could be introduced. The constraint of bit 3 is not required for the correction of the slice σ_0 because it makes no sense to correct values that have values outside the predicted range.

It is important to note here that the field `sigma0_model_flag` may be unreliable for discriminating between the inner and outer beams. In fact, it may happen that some of the beams that are classified as inner have incidence angle values comparable to those of the outer ones. In order to prevent such occurrences, the additional constraint that the inner beam incidence angle is lower than 50° is required. Actually, very few of such cases occur.

Field	Shape	Full name
sc_lat	(n_f,n_p,n_s)	sc latitude
sc_lon	(n_f,n_p,n_s)	sc longitude
sc_alt	(n_f,n_p,n_s)	sc altitude
x_pos	(n_f,n_p,n_s)	sc x-position ECEF
y_pos	(n_f,n_p,n_s)	sc y-position ECEF
z_pos	(n_f,n_p,n_s)	sc z-position ECEF
x_vel	(n_f,n_p,n_s)	sc x-velocity ECEF
y_vel	(n_f,n_p,n_s)	sc y-velocity ECEF
z_vel	(n_f,n_p,n_s)	sc z-velocity ECEF
cell_lat	(n_f,n_p)	cell latitude
cell_lon	(n_f,n_p)	cell longitude
cell_sigma0	(n_f,n_p)	cell σ_0
cell_azimuth	(n_f,n_p)	cell azimuth
cell_incidence	(n_f,n_p)	cell incidence angle
ant_azimuth	(n_f,n_p)	antenna azimuth
slice_snr	(n_f,n_p,n_s)	slice SNR
slice_kpc_a	(n_f,n_p,n_s)	slice kp a coefficient
slice_kpc_b	1	slice kp b coefficient
slice_kpc_c	1	slice kp c coefficient
slice_azimuth	(n_f,n_p,n_s)	slice azimuth
slice_incidence	(n_f,n_p,n_s)	slice incidence angle
slice_sigma0	(n_f,n_p,n_s)	slice σ_0
orbit_time	(n_f)	orbit time

Quality flag	Shape	Full name
frame_err_status	(n_f)	frame error status
frame_inst_status	(n_f)	frame instrument status
frame_qual_flag	(n_f)	frame quality flag
sigma0_mode_flag	(n_f,n_p)	σ_0 mode flag
sigma0_qual_flag	(n_f,n_p)	σ_0 quality flag
slice_qual_flag	(n_f,n_p)	slice quality flag

File attributes		
EquatorCrossingLongitude	1	Equator Crossing Longitude
orbit_inclination	1	Orbit inclination
rev_orbit_period	1	Orbit revolution period
orbit_semi_major_axis	1	Orbit semi-major axis
orbit_eccentricity	1	Orbit eccentricity

Table 1: List of fields used in this study. In the field "shape", n_f, n_p and n_s stand for "number of frames", "number of pulses" and "number of slices", respectively. n_p is equal to 100 and n_s to 8, while n_f may vary with the orbit. Its typical value is around 11240. The acronyms "sc" and "ECEF" stand for "spacecraft" and "Earth-Centered Earth-Fixed", respectively.

4 Methodology

4.1 impact of the intra-egg bias on $\hat{K}_p$

The methodology used to estimate the noise of the slice σ_0 has been extensively described in [8], therefore, it will not be reported here again in detail. Only the most relevant aspects are listed:

- five different levels of σ_0, approximately corresponding to wind speeds equal to 5, 7.5, 10, 12.5 and 15 ms^{-1}, are estimated by means of the geophysical model function (GMF) NSCAT4DS, for each beam;

- The measurements are binned around these five levels ± 0.5dB;

- The deviations w.r.t. the egg σ_0 are computed;

- The variance of the noise is estimated by means of the root mean square (RMS) formula. The value of egg σ_0 can reasonably be assumed to be the expected value; therefore, the obtained RMS can be considered as the noise variance plus the square of the bias induced by the difference in the incidence angle between the centroids of the slice and the egg.

Instead, the methodology used to assess the impact of *intra* egg biases induced by the variability of the incidence angle is described. The effective σ_0 bias induced by the difference between the slice and the egg centroids depends on the wind direction. This information is, of course, not available. However, we can estimate the bias in the worst-case scenario (WCS), by using the GMF as in Equation 4.1, where θ is the incidence angle, ϕ the relative wind direction w.r.t. the antenna beam, U is the wind speed, $N4DS$ stands for the GMF NSCAT4DS, i is the slice index, j is the sample index and $sgn(i)$ equals -1 for the slices with indices up to 4 (the farthest ones) and 1 for the remaining slices (see Figure 2). In fact, the GMF is a monotonically decreasing function of θ. That is, if $\theta^{i,j}$ is higher (less) than θ^j_{egg} as for the first four slices (last four), σ_0^i is expected to be less (higher) than $\sigma_{0,egg}$, if we accept that the geophysical variability in the egg is negligible. The figure 2 shows the inner beam -3dB contours of the spatial response function (SRF) of the slices in a region in southern Italy, together with some additional information that can help to better understand the acquisition geometry of QuikSCAT. The slice indices are reported in the contours with a 0-based numbering, while the satellite track is depicted with a black arrow centered on the 7th slice, to emphasize that the antenna azimuth angle is around 190°. Finally, the slice centroids are represented by black dots, whereas the egg centroid is represented by a red triangle.

WCS means that we consider the relative wind direction with the largest absolute deviation from σ_0^{egg}. The solid line of figure 3 shows the expected value of the deviation of σ_0 from σ_0^{egg} in linear units (LU), for the inner aft slice with index 0 for a wind speed equal to 5 ms^{-1}, as predicted by NSCAT4DS, throughout the entire orbit with ID 40651. The average value of the solid line is represented by the dashed line. Note that the values are all negative, in agreement with what is expected. In this case, the WCS is represented by the deviation at $\phi = 5^o$, which is much larger (in absolute value) than the average value. This value can reasonably be considered to be the upper limit of the bias in this specific case. The maximum bias evaluated throughout the orbit is considered (4.1). The ratio of this value to the expected value of σ_0 gives the upper limit of the impact of such a bias on $\hat{K}_p$ in the same units.

$$b_i = sgn(i)max_j[max_\phi|N4DS(U,\theta^{i,j},\phi) - N4DS(U,\theta_{egg}^j,\phi)|] \qquad (4.1)$$
$$\forall i \in 0,\ldots,7$$
$$\forall j \in 1,\ldots,N$$
$$sgn(i) = -1 \forall i \in 0,\ldots,3$$
$$sgn(i) = 1 \forall i \in 4,\ldots,7$$

4.2 Reformulation of the LCR estimation

In [5] the LCR index is calculated as the ratio of the number of land classified points to the total points encompassed by the -3dB slice contour. In Section 5 it will be shown that this definition may lead to severely underestimated LCR values. In fact, the -3dB contour represents the majority of the incoming energy, but the contribution from the peripheral part of the footprint may be relevant, especially if the σ_0 contrast between land and sea is high. For this reason, the definition of LCR proposed in [1] has been implemented, which is hereafter reported for the sake of completeness.

$$LCR = \frac{\sum_{xy} L_{xy} S_{xy}}{\sum_{xy} S_{xy}} \qquad (4.2)$$

In this new implementation, which is called "full", the land/sea mask is interpolated at the grid points where the SRF is estimated. Then, equation 4.2 is applied. The black line of Figure 4 shows the same -3dB SRF contour for the slice with index 2 depicted in Figure 2. The red lines represent the contours of -30dB, -20dB and -10dB, showing that, in this case, the
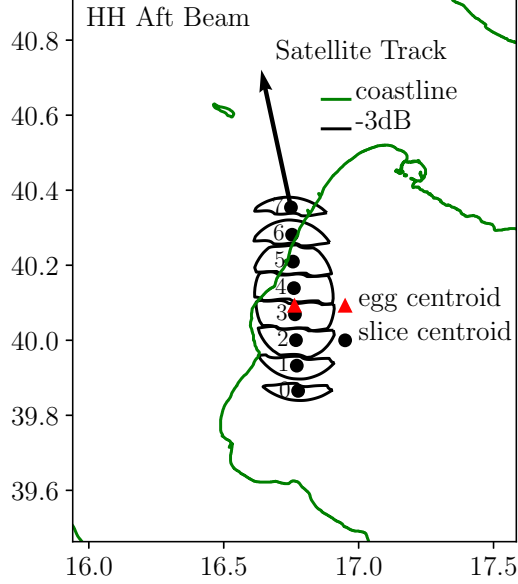
Figure 2: QuikSCAT inner egg

contamination of the land may be almost 10%, even if the contour of -3dB does not cover any piece of land.

4.3 LCR-based σ_0 correction scheme

The LCR-based σ_0 correction scheme implemented in this study is based on the hypothesis that the dependency of σ_0 on LCR is linear, as indicated in equation 4.3

$$\sigma_0 = af + \sigma_0^{SEA} \tag{4.3}$$

where f stands for LCR. The scheme proposed here is identical to the one described in [4]. Therefore, only the most relevant aspects are reported here. For more details, the reader can refer to it. The slope of 4.3 is regressed with the least-square method together with the offset (b), which represents the average σ_0^{SEA} of the data set. Their variances (σ_a^2 and σ_b^2) and the regression error (σ_e^e) are evaluated. The formula of σ_e^2, σ_a^2 and σ_b^2 are reported here for the sake of completeness:
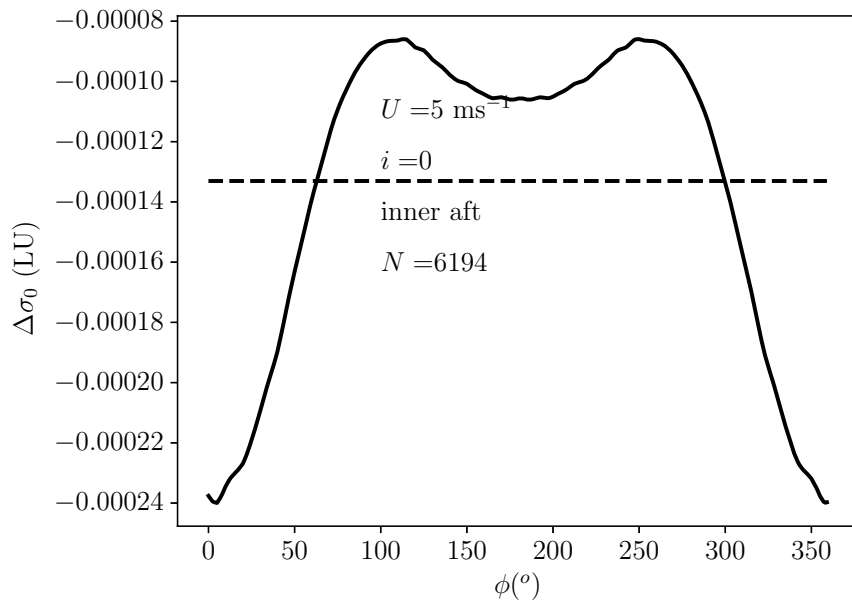
Figure 3: Solid line: expected σ_0 deviation from σ_0^{egg} for the inner aft slice with index 0 as a function of the relative wind direction (ϕ) simulated with NSCAT4DS at a wind speed equal to 5 ms^{-1} in linear units (LU). Dashed line: average value of the solid line. The dataset refers to the orbit with ID 40651, and consists of 6194 samples.
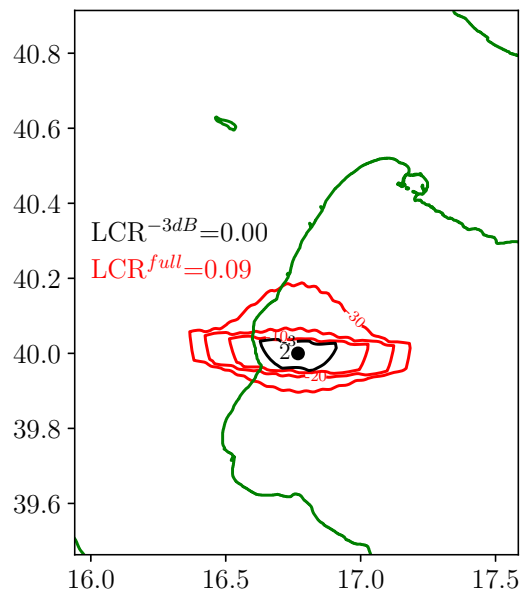
Figure 4: Black line: SRF contour -3 dB for the inner beam slice with index 2, the same as in Figure 2. Red lines: -30, -20 and -10 dB contours of the SRF. The LCR^{full} (LCR^{-3dB}) is reported in red (black) in the panel.

$$\sigma_e^2 = \frac{n}{n-2} \left(C_{\sigma\sigma} - 2aC_{f\sigma} + a^2 C_{ff} \right) \tag{4.4}$$

$$\sigma_a^2 = \frac{\sigma_e^2}{nC_{ff}} \tag{4.5}$$

$$\sigma_b^2 = \sigma_a^2 M_{ff} \tag{4.6}$$

where C_{xy} stands for the covariance of the variables x and y, M_{xx} represents the second order moment of the variable x, σ stands for σ_0 and n is the total number of samples. This parameter is used for QC and to set the weights in a Gaussian averaging procedure, as described in Subsection 4.4. Once a is known, equation 4.3 is inverted to estimate the corrected ("SEA") σ_0:

$$\sigma_0^{SEA} = \sigma_0 - af \tag{4.7}$$

All slice σ_0s that belong to the 5x5 matrix of WVCs surrounding the WVC where the correction is applied are used for regression. Figure 5 may help clarify this. This picture shows a map of slice σ_0s in offshore the Netherlands, with a logarithmic gray colorbar. Note that the σ_0s close to the coast are lighter than those in open sea, highlighting that land contamination is likely present in these acquisitions. The red-framed WVC represents the WVC where the correction is applied. All σ_0s that belong to the given WVC and the surrounding 24 are used for the regression. The regression is performed onlyt if there are at least 3 samples with $f \leq f_T$. After the correction, σ_0s with $f > f_T$ are discarded. In this analysis, two values of f_T are considered: 0.2 and 0.5.

4.4 Integration of σ_0

Before integration, all slice σ_0s are binned on a regular WVC grid with a spacing of 12.5 km. Slices σ_0s are integrated with a weighted averaging procedure, according to equation 4.8.

$$\sigma_{0,ij}^{pv} = \frac{\sum_k w_{ijk}^{pv} \sigma_{0,ijk}^{SEA,pv}}{\sum_k w_{ijk}^{pv}} \tag{4.8}$$

$$\forall p \in \{H, V\}$$
$$\forall v \in \{fore, aft\}$$
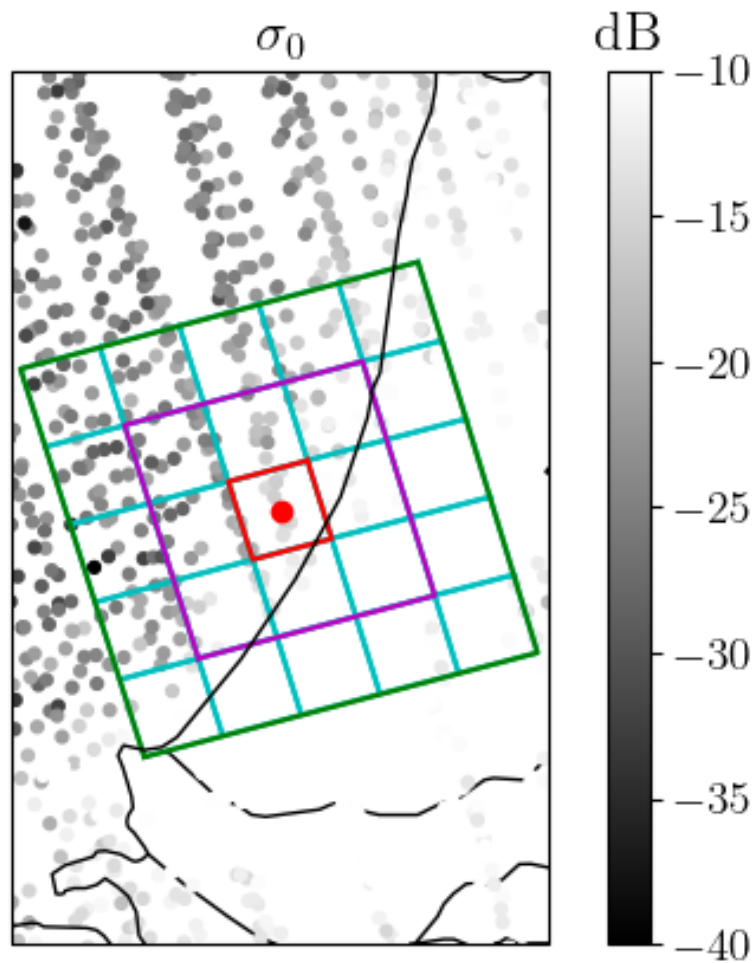$$\forall k \in \{1, \ldots, N_{ij}^{pv}\} \tag{4.9}$$

Figure 5: Map of slice σ_0s offshore the Netherlands. The red frame represents the WVC where the σ_0 correction is applied, and the red circle is its centroid. The green-framed (magenta-frame) box represents the 5x5 (3x3) WVC matrix used for the regression with the LCR^{full} (LCR^{-3dB}) method.

where $\sigma_{0,ij}^{pv}$ stands for integrated σ_0 with polarization p (H or V), view v ($fore$ or aft), and WVC indices i,j, $\sigma_{0,ijk}^{SEA,pv}$ is the k-th corrected slice σ_0 of N_{ij}^{pv}, and w_{ijk}^{pv} is its corresponding weight.

Four different weighting strategies are applied in this study:

- boxcar averaging ($w_{ijk}^{pv} = 1$)

- LCR averaging ($w_{ijk}^{pv} = 1 - f_{ijk}$)

- K_p averaging ($w_{ijk}^{pv} = \frac{1}{K_{p,ijk}^2}$)

- Gaussian averaging $w_{ijk}^{pv} = e^{-\frac{\sigma_{0,ijk}^{pv} - a_{ij}^{pv} f_{ijk}^{pv} - \sigma_{0,ij}^{SEA,pv}}{F\sigma_{e,ij}^{2,pv}}}$

Gaussian averaging assigns the weight according to the vertical distance of the slice σ_0 from the regression line (the corrected value). Note that the lower F, the lower is the weight assigned to the outliers. In this analysis, $F = \frac{1}{2}$.

Finally, the new WVC$_{ij}$ centroid is evaluated according to Equations 4.10:

$$\phi_{ij} = \frac{\sum_p \sum_v \sum_k w_{ijk}^{pv} \phi_{ijk}^{pv}}{\sum_p \sum_v \sum_k w_{ijk}^{pv}}$$

$$\lambda_{ij} = \frac{\sum_p \sum_v \sum_k w_{ijk}^{pv} \lambda_{ijk}^{pv}}{\sum_p \sum_v \sum_k w_{ijk}^{pv}}$$

(4.10)

with ϕ_{ij} and λ_{ij} the latitude and longitude of the WVC centroid, respectively.

5 Results and discussion

## 5.1 Estimation of $\hat{K}_p$ on a larger dataset

The circles in each plot of figure 6 represent the median of the values K_p ($\tilde{K}_p$) provided in the QuikSCAT full-resolution files w.r.t. the slice index, for each of the four pol-view flavors, namely H-pol aft and fore (HHA and HHF), V-pol aft and fore (VVA and VVF), and the total number of samples is reported by the flavor. Instead, the crosses represent the estimates ($\hat{K}_p$) obtained with the methodology proposed in this study. The 68% (95%) confidence intervals (c.i.) of the values K_p are indicated with the solid (dashed) lines. The wind speed values approximately corresponding to the five σ_0 levels used for the estimates are reported in the caption. Finally, the right (left) column reports the results evaluated on the orbit with ID 40651 (all the 14 orbits dated 10th of April 2007). Some thoughts are apparent, some of which were already noted in [5]: a) H-pol acquisitions are noisier than those V-pol; b) H-pol fore acquisitions are noisier than H-pol aft; the reason is not yet clear; c) H-pol acquisitions with the indices 6 and 7 (see Figure 2) are noisier than the symmetric indices 0 and 1; neither is this reason clear; d) the H-pol acquisitions with indices 6 and 7 are outside the 68% c.i.; for mid-high σ_0 levels they are even outside the 95% c.i., stating that the differences between $\hat{K}_p$ and $\tilde{K}_p$ are meaningful and that K_p levels are largely underestimated; e) inner V-pol acquisitions have lower levels of noise than reported in the files, while the opposite happens for those outer; f) finally, the statistics relating to a single orbit are rather similar to those evaluated on the entire set of 14 orbits dated 10th of April 2007, showing that these results are not related to any particular geophysical conditions.

The solid lines (dashed) of Figure 7 show the average (WCS) intra-egg biases induced by the variation in the angle of incidence. It is apparent that the trend is rather linear; therefore, we expect that they will compensate during the integration procedure. In addition, the biases are larger for the H-pol acquisitions and for the aft view. This is in agreement with the values of the expected deviations of the slice incidence angles w.r.t. the egg incidence angle, as reported in Table 2. Note that the standard deviations of the deviations follow the same trend as their expected values.
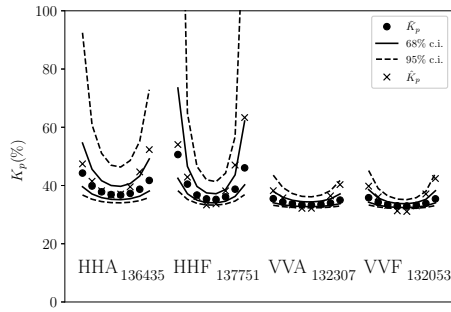
Figure 8 shows the impact of the intra-egg biases on $\hat{K}_p$ in WCS. All values are less than 7%, and are higher for H-pol acquisitions. Note that these figures refer to the WCSs. Even under these strict conditions, the differences between $\hat{K}_p$ and $\tilde{K}_p$ are meaningful; therefore, the conclusions stated above are still valid.
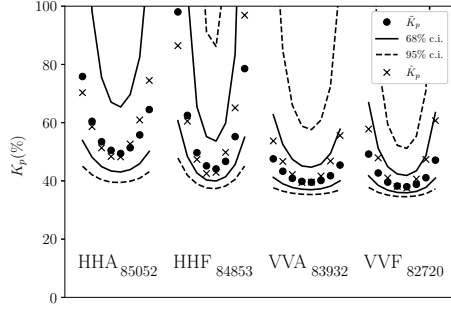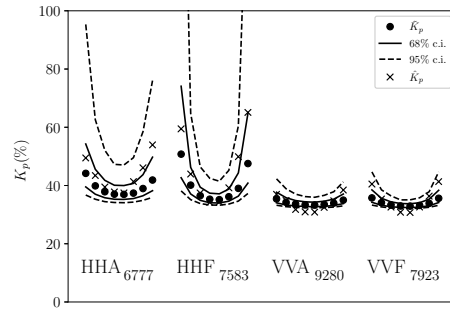
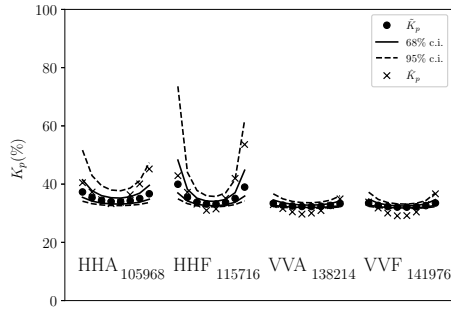(a) $U \approx 5 \text{ ms}^{-1}$
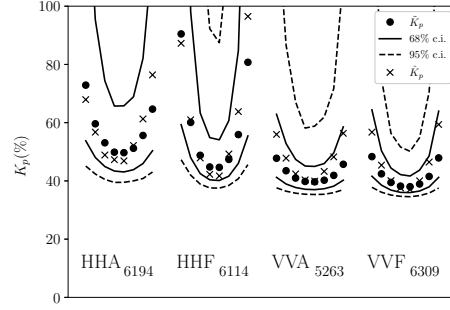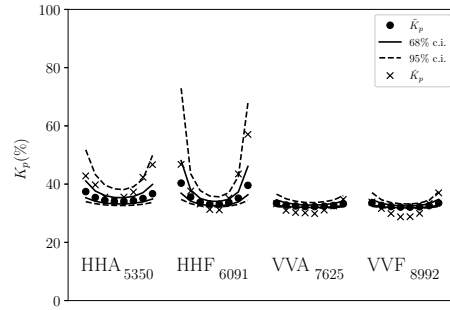
(b) ID 40651. $U \approx 5 \text{ ms}^{-1}$
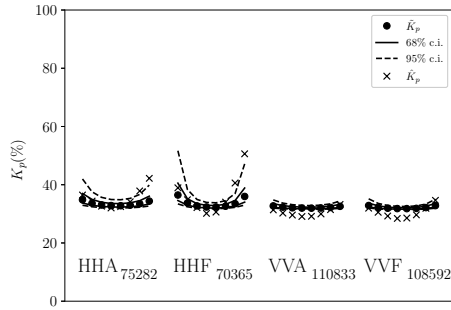
(c) $U \approx 7.5 \text{ ms}^{-1}$

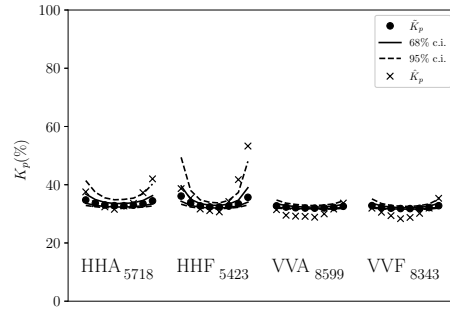(d) ID 40651. $U \approx 7.5 \text{ ms}^{-1}$

(e) $U \approx 10 \text{ ms}^{-1}$

(f) ID 40651. $U \approx 10 \text{ ms}^{-1}$

(g) $U \approx 12.5 \text{ ms}^{-1}$
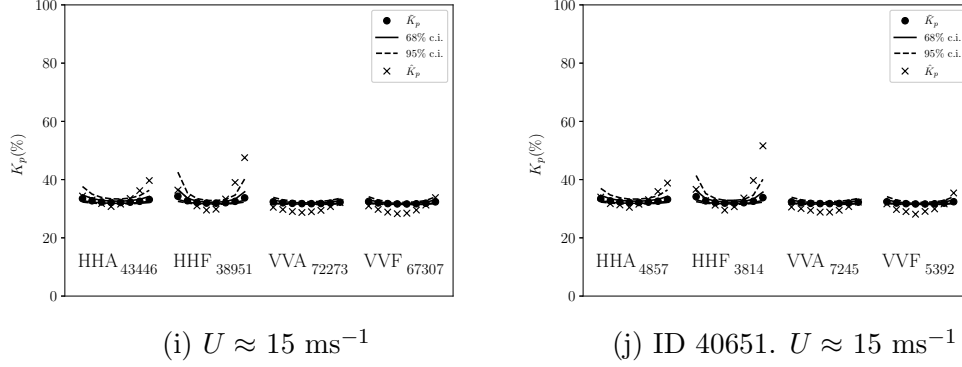
(h) ID 40651. $U \approx 12.5 \text{ ms}^{-1}$

(i) $U \approx 15 \text{ ms}^{-1}$ (j) ID 40651. $U \approx 15 \text{ ms}^{-1}$

Figure 6: In each plot, the circles represent the median of K_p values ($\tilde{K}_p$) provided in the QuikSCAT FR files w.r.t. the slice index, for each of the four pol-view flavours, and for the σ_0 level corresponding approximately to the wind speed indicated in the caption; The 68% (95%) confidence intervals of K_p are represented with solid (dashed) lines; Estimates of K_p ($\hat{K}_p$) are depicted with crosses; The total number of samples is reported by the flavour. The right (left) column reports the results evaluated on the orbit with ID 40651 (all orbits dated 10th of April 2007).

slice #	HHA	HHF	VVA	VVF
0	0.68±0.09	0.95±0.15	0.56±0.08	0.67±0.09
1	0.48±0.09	0.66±0.13	0.40±0.08	0.48±0.09
2	0.26±0.09	0.37±0.12	0.24±0.08	0.29±0.08
3	0.05±0.09	0.07±0.11	0.08±0.08	0.09±0.08
4	-0.16±0.09	-0.23±0.12	-0.08±0.08	-0.11±0.08
5	-0.38±0.09	-0.54±0.13	-0.24±0.08	-0.31±0.08
6	-0.60±0.09	-0.85±0.16	-0.41±0.08	-0.51±0.08
7	-0.82±0.10	-1.17±0.19	-0.57±0.08	-0.72±0.10

Table 2: Expected values of the deviations of the slice incidence angle w.r.t. the egg incidence angle in degrees $\pm$ their standard deviations, for the orbit with ID 40651.
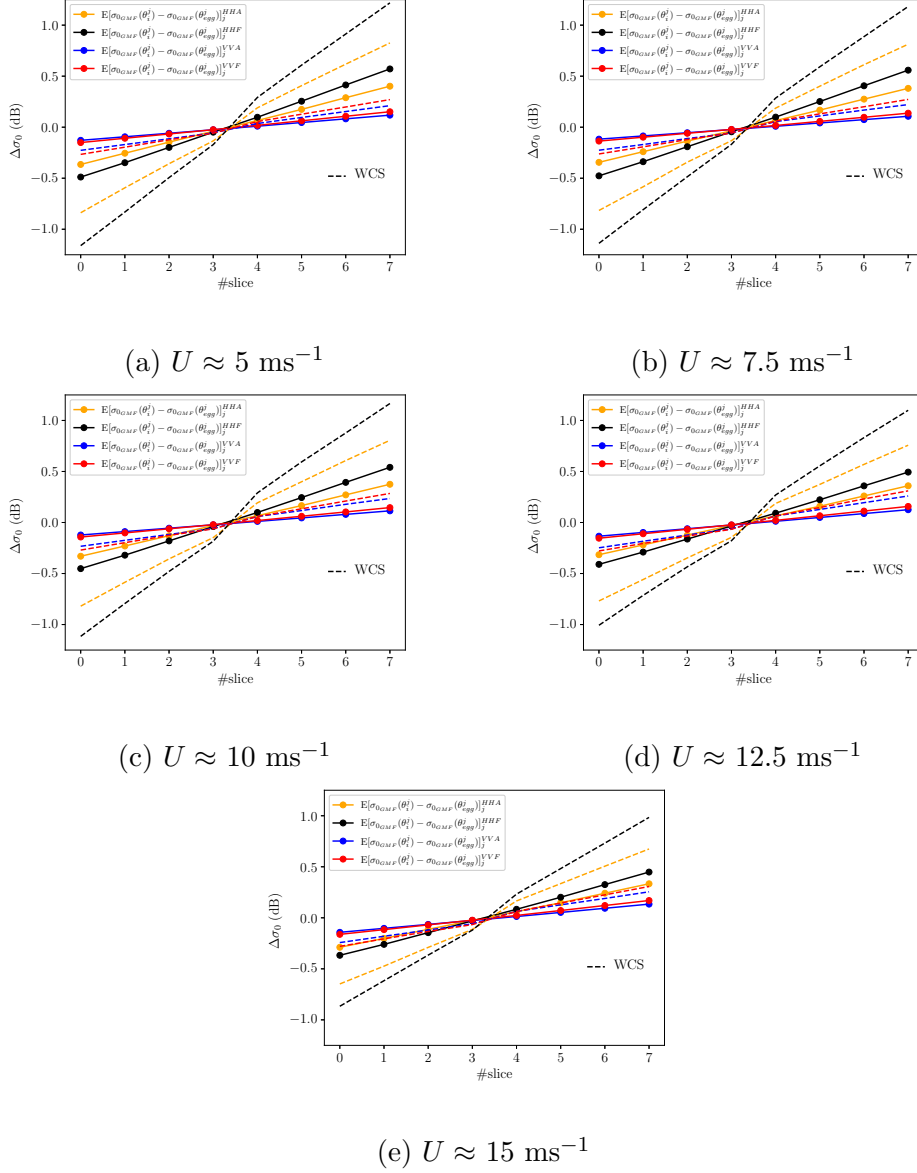
(a) $U \approx 5$ ms^{-1}

(b) $U \approx 7.5$ ms^{-1}

(c) $U \approx 10$ ms^{-1}

(d) $U \approx 12.5$ ms^{-1}

(e) $U \approx 15$ ms^{-1}

Figure 7: Solid (dashed) lines: average (maximum) intra-egg σ_0 bias induced by the incidence angle variations w.r.t. the slice index, for the four pol-view flavors, and for the σ_0 level corresponding approximately to the wind speed indicated in the caption. The estimates refer to the orbit with ID 40651. WCS stands for Worse Case Scenario.
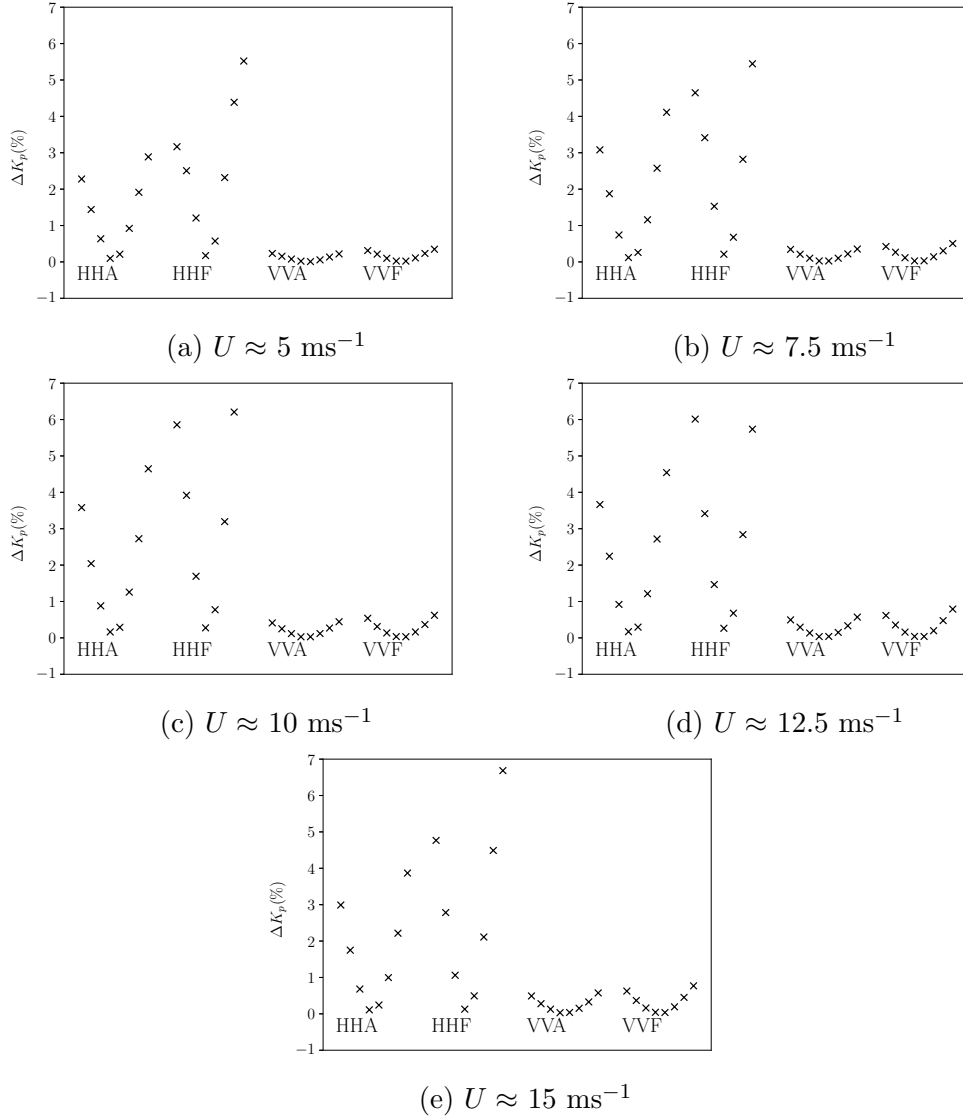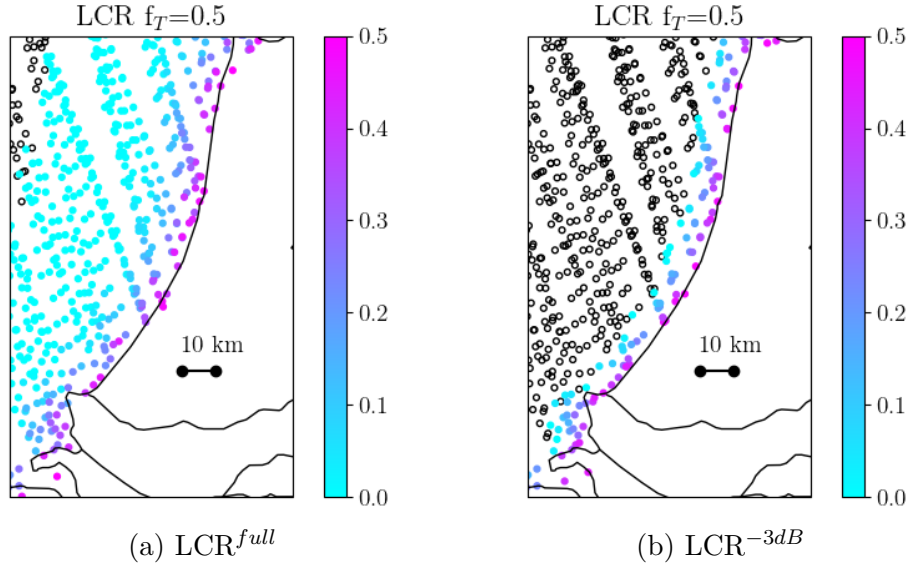
(a) $U \approx 5$ ms^{-1}

(b) $U \approx 7.5$ ms^{-1}

(c) $U \approx 10$ ms^{-1}

(d) $U \approx 12.5$ ms^{-1}

(e) $U \approx 15$ ms^{-1}

Figure 8: Impact of the intra-egg biases on $\hat{K}_p$ w.r.t. slice index, for each of the four pol-view flavors, and for the σ_0 level corresponding approximately to the wind speed indicated in the caption, in the WCS. The estimates refer to the orbit with ID 40651.

Figure 9: Left (right): LCR map offshore The Netherlands obtained with the LCR^{full} (LCR^{-3dB}) method. Slices with LCR equal to 0 are represented by black-framed empty circles.

5.2 LCR-based σ_0 correction

Figure 9a (9b) shows the LCR offshore the Netherlands obtained with the LCR^{full} method (LCR^{-3B}). It is apparent that land contamination affects a much larger offshore strip if the LCR^{full} method is used instead of the LCR^{-3dB}. To emphasize this aspect, the slice centroids with an LCR equal to 0 are represented by empty black-framed circles. Figure 10a (10b) shows the scatter plot of slice σ_0s in linear units that are assigned to the WVC framed in red of Figure 5 w.r.t. LCR obtained with the LCR^{full} (LCR^{-3dB}) method. The number of samples depicted in Figure 10a is higher than in Figure 10b. In fact, in the former case, all the slices that fall into the 5x5 WVC matrix surrounding the red-framed WVC are used, while only those that fall into the surrounding 3x3 WVC matrix are used in the second case (the magenta-framed box in Figure 5). It does not make much sense to use a larger WVC matrix if the LCR^{-3dB} method is applied, since many slices with an LCR equal to 0 or 1 would be added to the scatter plot, with consequent worse slope fit.

In Figure 10, the slice σ_0s are segregated according to their pol-view. It is apparent that H-Pol acquisitions are noisier than those V-Pol, in line with the previous results. Trends are quite similar in both cases. However, it
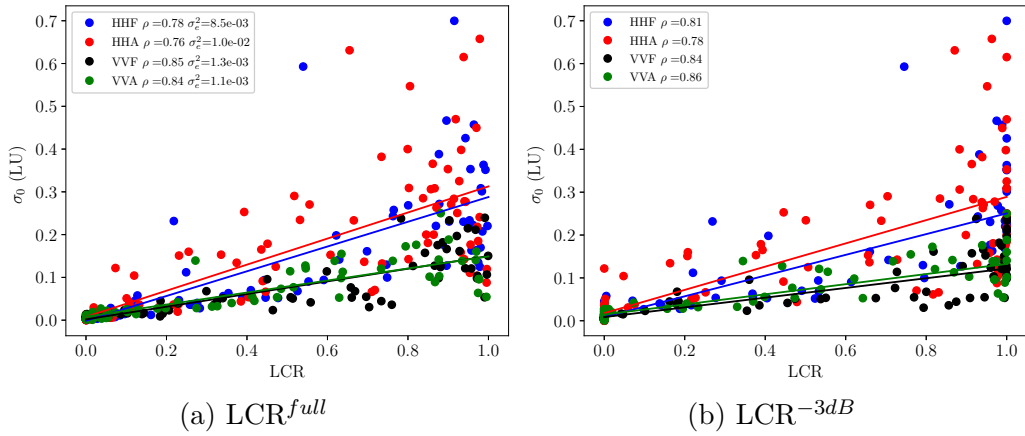
Figure 10: Left (right): scatter plot of σ_0s in linear units w.r.t. LCRs obtained with the LCR^{full} (LCR^{-3dB}) method, for the WVC depicted with the red circles in Figure 5. The points are segregated according to the pol-view flavors. The fitting curves are reported with the same color coding and the correlation coefficients are reported by the flavor string. The value of the corresponding σ_e^2 is reported in the legend of the plot on the left. This information was not available at the stage of development of the software when the case depicted in the plot on the right was handled.

is evident that the points tend to cluster around LCR equal to 0 and 1 in Figure 10b. This suggests that some points with an LCR equal to 0 (1) are contaminated (not completely covered by land).

Figure 11a shows a map of the measured σ_0s in the same area as Figure 9, while Figure 11b (11c) shows a map of the corrected σ_0s obtained with the LCR^{full} (LCR^{-3dB}) method; It is apparent that the coastal band within ≈ 20 km of the shoreline is contaminated by land, since the high coastal values are probably not due to specific geophysical conditions. Furthermore, the correction based on the LCR^{full} method appears to be more effective than the one based on the LCR^{-3dB}. In fact, in the former case, the values of σ_0 appear to be lower than in the second case. This is particularly evident in the magenta-framed box. However, negative occurrences of σ_0 are much more numerous than in the second case. This is, of course, an unwanted side effect of correction, which should be further investigated in the future.

Figure 13a (13b) shows the distribution of the number of samples used for slope regression, for each flavor pol-view when f_T is set to 0.5 (0.2). The numbers next to the flavor string represent the total number of WVCs where the regression is performed. Given a flavor pol-view, the total number of WVCs on which the regression is performed is greater if f_T is set to 0.5. In

fact, many WVCs that are very close to the shoreline have no slices with $f \leq 0.2$. As mentioned above, in such cases, regression is not performed. Note that the set of WVCs in which regression is performed with $f = 0.2$ is a subset of that with f = 0.5. In such occurrences, the regression coefficients are exactly the same. Even the corrections are exactly the same. In fact, f_T is used to discriminate the cases where corrections will be applied, but the samples assigned to the WVC to fit the curve do not depend on f_T. The only difference is that coastal sampling is poorer when f_T is set to 0.2. In fact, Figure 12 is exactly the same as Figure 11b but f_T is set to 0.2. The values are identical, but the coastal band within ≈ 10 km is not sampled.

The distributions shown in Figures 13a and 13b are similar to each other. Furthermore, their moda is never less than ≈ 80, and the lowest number of samples is not less than ≈ 70. Two aspects are not yet clear: a) the moda is higher for H-pol acquisitions; b) it is slightly higher for the fore view.

Figure 14a shows the distribution of the slope coefficient (a) for each pol-view flavor, when f_T is set to 0.5, while Figure 14b shows the distribution of its error variance. In general, the slope for H-pol acquisitions is higher than for those V-pol. This is in agreement with the specific case shown in Figure 10. The distribution of σ_a^2 is a decaying function; therefore, no specific threshold values are recommended to filter poor-quality regressions. If a threshold value equal to 0.001 were chosen, the percentage of WVCs rejected would be represented by the numbers by the flavor in the legend of Figure 14b. The results relating to f_T equal to 0.2 are very similar and, therefore, are not shown for the sake of brevity. In the following, only the results for $f_T = 0.5$ are shown.

Figure 15a shows the distribution of the offset coefficient for each pol-view flavor, while Figure 15b shows the distribution of its error variance. In this case, no appreciable differences occur among the pol-view flavors. The distribution of σ_b^2 is similar to that of σ_a^2 but for the decaying rate. Therefore, the same considerations apply: no threshold value is suggested to filter poor-quality regressions.

Finally, Figure 16 shows the distribution of the regression error for each pol-view flavor. Once again, the trend of the distribution is monotonically decreasing, and no useful threshold values are suggested to filter poor-quality regressions. However, if the threshold value equal to 0.005 were chosen, the percentage of rejected WVCs would be the number reported by the flavor in the legend. Furthermore, the percentage of retained pol-view triplets useful for wind retrievals would be slightly less than 87%.

Figure 17 shows the distribution of the measured σ_0s in the interval [-50, 5] dB, segregated according to their distance from the coast, in a 10 km step, up to 100 km, for each flavor. Some figures are displayed in the panel, from
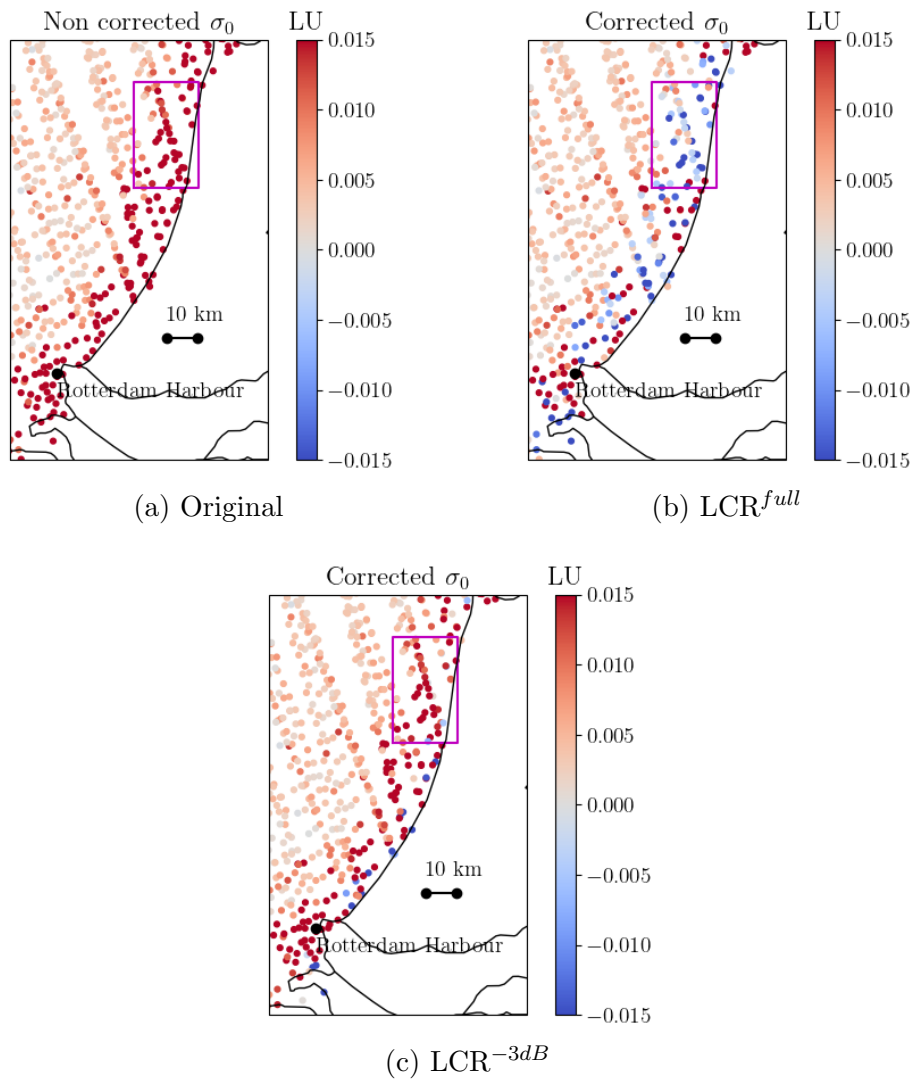
(a) Original

(b) LCR^{full}

(c) LCR^{-3dB}

Figure 11: Top left: σ_0 map offshore The Netherlands before any corrections. Top right (bottom center): σ_0 after correction with the LCR^{full} (LCR^{-3dB}) method.
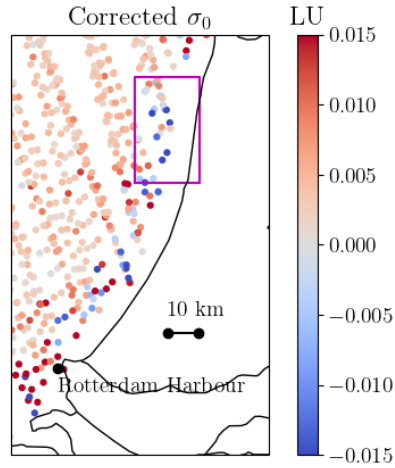
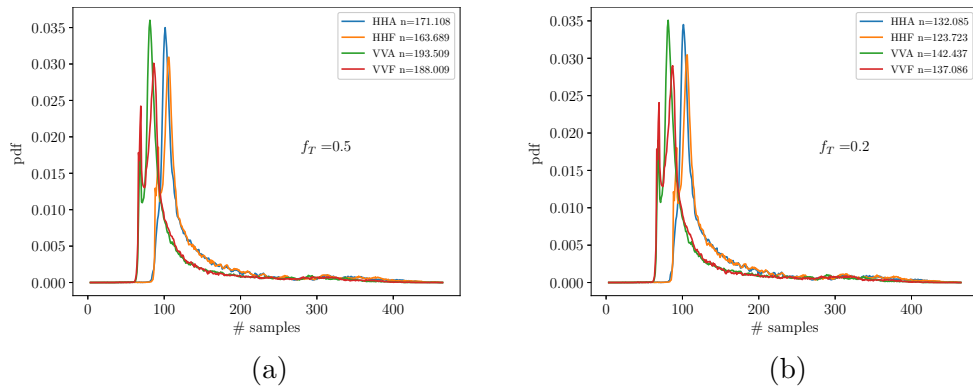Figure 12: Corrected slice σ_0 map offshore The Netherlands for f_T equal to 0.2.

Figure 13: Left (right) plot: pdf of the number of samples used for the slope regression when f_T is set to 0.5 (0.2), for each pol-view flavor. The number next to the flavor string in the legend represents the total number of WVCs for which the regression is performed.

(a) pdf of the slope coefficient (a).

(b) pdf of the variance of a (σ_a^2).
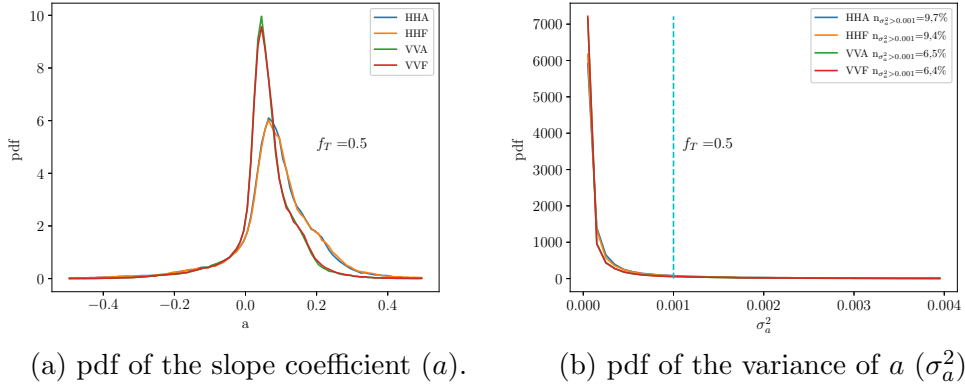
Figure 14: Left (right): pdf of the slope coefficient (its error variance), for each pol-view flavor. The numbers next to the flavor in the legend represent the percentage of rejected occurrences in case where the threshold value for σ_a^2 equal to 0.001 were chosen.
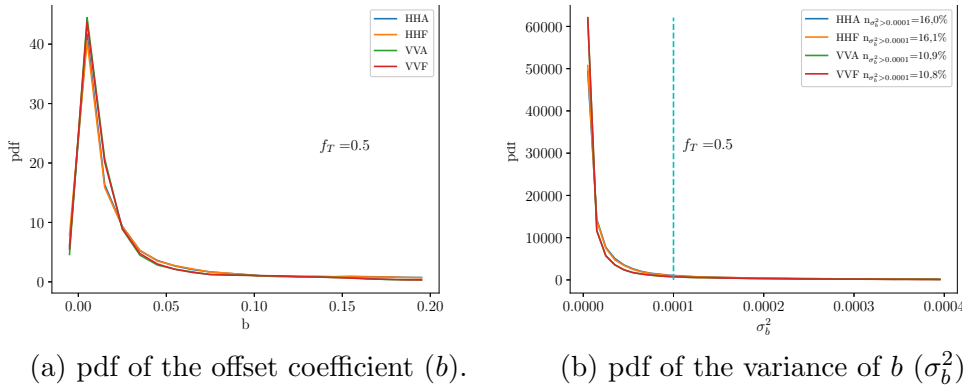

(a) pdf of the offset coefficient (b).

(b) pdf of the variance of b (σ_b^2).

Figure 15: Left (right): pdf of the offset coefficient (its error variance), for each pol-view flavor. The numbers next to the flavor represent the percentage of rejected occurrences in case where the threshold value for σ_b^2 equal to 10^{-4} were chosen.
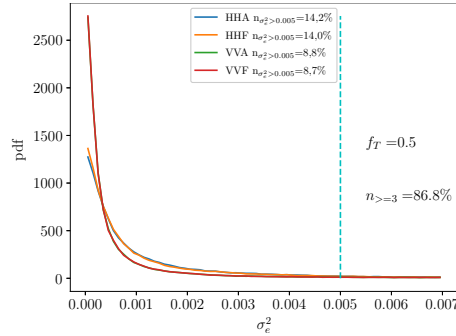
Figure 16: pdf of the error variance (σ_e^2). The numbers next to the flavor strings represent the percentage of rejected occurrences in the case where the threshold value for σ_e^2 equal to 0.005 were chosen.

top to bottom: a) the total number of samples shown; b) the number of negative values; c) the total number of samples outside the interval [-50, 5] dB; d) the sum of a), b) and c) in red.

Figure 18 is identical to Figure 17 but for the corrected σ_0s. Some things are apparent: a) the two most affected curves by correction are those within 20 km of the shoreline, as expected (blue and orange); b) both curves shift towards lower values. This aspect is also expected, as land contamination often increases the value of σ_0; c) the number of negative σ_0s increases sensibly ($\approx 70\%$ and 100% more for H-Pol and V-Pol, respectively), but if the focus is on the 50 km strip closer to the coast, the number of total negative values increases from 319,640 to 818,319 ($\approx 250\%$ more). This number may seem high, but it is expected. In fact, if one looks at the scatter plot of Figure 10 and ideally brings each point towards LCR equal to 0 along the fitted curve, a large number of points would fall into the negative part of the plot, considering also that the offset is generally very low (Figure 15a). This is due to the high noise that affects the QuikSCAT measurements. Consider that K_p is never less than $\approx 30\%$ and that, in low wind regimes, it may be much higher than 100%, given its very high dispersion around median values (see Figure 6b). Therefore, this aspect is intrinsic to the correction methodology applied in this study.

Figure 19 is the same as Figure 18 when QC is applied to σ_e^2. Some additional numbers are reported in the panels: the number of positive values that do not pass the QC in the interval shown, the total number of negative values outside the interval shown that pass the QC, the total number of positive values outside the interval shown that pass the QC, the total number of negative values that do not pass the QC, the total number of positive values outside the interval shown that do not pass the QC. It is apparent
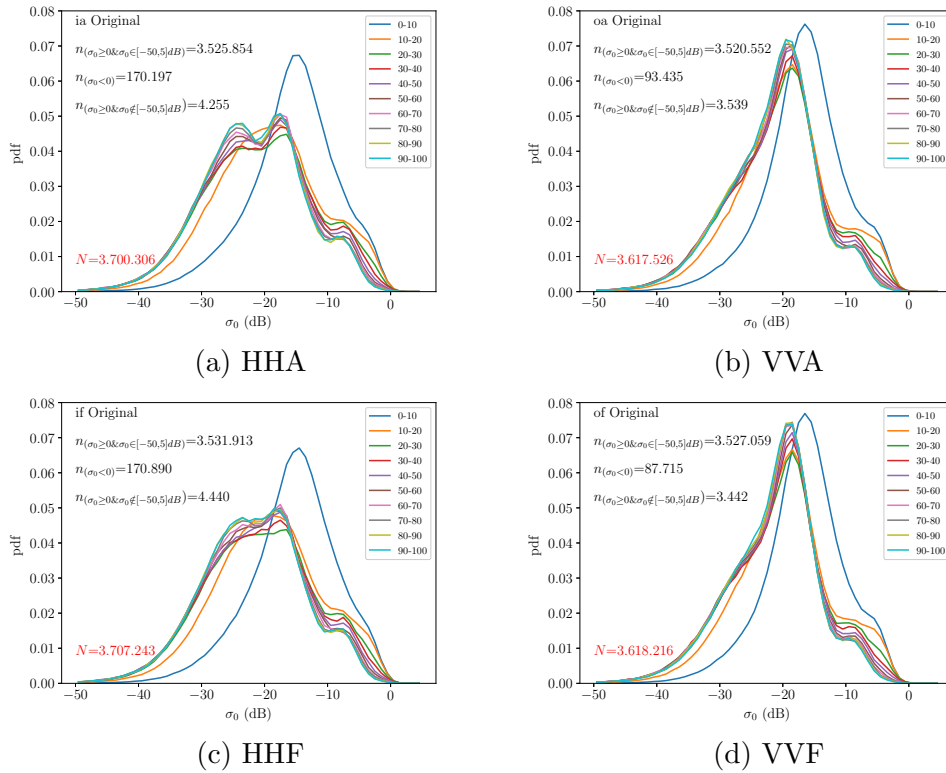
(a) HHA

(b) VVA

(c) HHF

(d) VVF

Figure 17: pdf of the slice σ_0s before correction in the interval $[-50, 5]$ dB, segregated according to the distance to the coastline, in a step of 10 km, up to 100 km. Top-down numbers: a) the number of samples shown; b) the number of negative values; c) the number of samples outside the interval $[-50, 5]$ dB. The sum is reported in red in the panel.
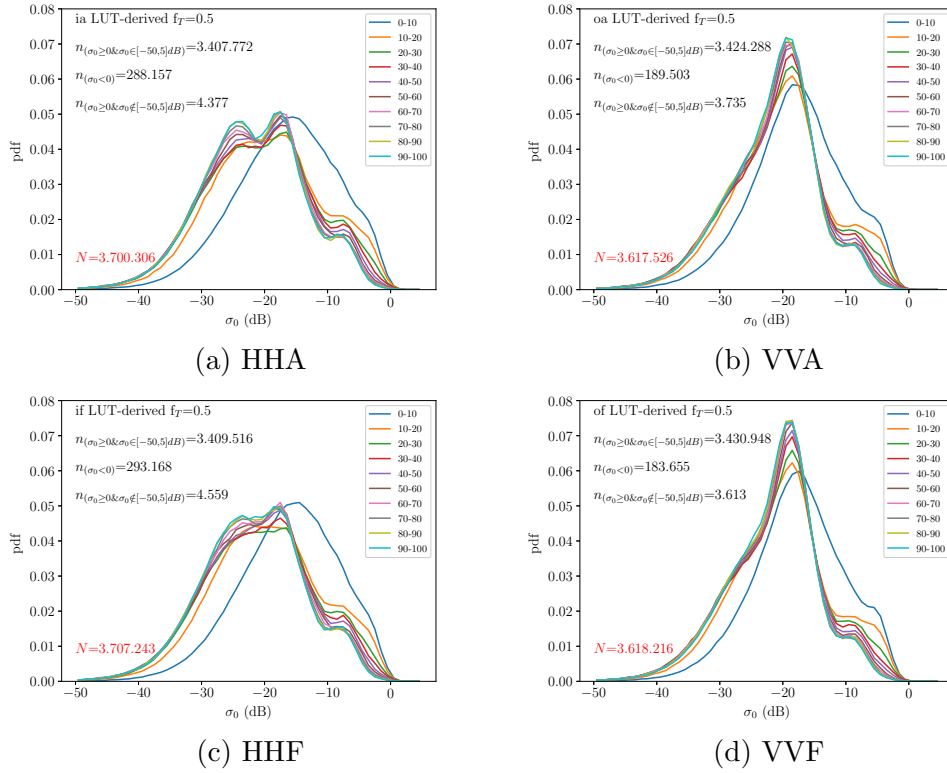
Figure 18: pdf of the slice σ_0s after correction in the interval $[-50, 5]$ dB, segregated according to the distance to the coastline, in a step of 10 km, up to 100 km. Top-down numbers: a) the number of samples shown; b) the number of negative values; c) the number of samples outside the interval $[-50, 5]$dB. The sum is reported in red in the panel.

that, when QC is applied to σ_e^2, the number of values of σ_0 in the interval $\approx$ [-10, 0] dB is sensibly reduced. Figure 20 shows the distribution of rejected σ_0s for each pol-view flavor when the regression error must not exceed 0.005. The distribution is segregated according to the distance to the shoreline. The most rejected σ_0s are in the interval [-20, 0] dB, with a peak in the interval [-10, 0] dB.

Finally, Figure 21a (21b) shows the map of the measured (corrected) slice σ_0s offshore western Sicily. It is also apparent in this case that the correction is effective (see the magenta-framed box), even if some residual contamination seems to be present very close to the shoreline.

5.3 Integrated σ_0^{pv}

Figure 22 (23) shows the integrated σ_0 for each pol-view flavor, before any corrections are applied, offshore western Sicily (The Netherlands). Before integration, all slices with LCR greater than 0.02 are rejected, as required for regular open ocean wind vector field retrievals. As can be seen, coastal sampling is very poor, as expected. Some points lie closer to the coast than others, because the orientation of the slices may be particularly favorable in such cases.

The black-framed empty circles represent the WVCs for which the integrated values are missing. This occurs especially for Figure 23b. This occurs because of a double negative effect that Figure 24 can help to understand. Figure 24a represents the slice centroids segregated according to their pol-view flavor off-shore the Netherlands. The black circle represents the WVC centroid surrounded by the cyan circle in Figure 23b, and the black frame represents its area. All the slices falling in this black frame are used to calculate σ_0^{pv} for that specific WVC. Figure 24b represents only the slices that the selection algorithm assigns to this WVC. Two things are apparent: a) the linear dimension of the WVC is comparable to the distance between tw0 consecutive streaks of the same color. The black-framed empty circles in Figure 23b fall approximately between two consecutive VVA streaks; b) the algorithm "misses" the unique red point (VVA), which apparently falls in the lower right corner of the WVC frame. This is of course a bug in the tool seawinds l1b bufr, which is part of the code PenWP, and should be fixed in the future. Note that QC does not play any role here. In fact, all acquisitions are shown in Figure 24a, before any QC is applied.

Figures 25 (29), 26 (30) and 27 (31) show the boxcar, K_p and LCR-averaged σ_0s for each pol-view flavor, in the area offshore western Sicily (The Netherlands). In this case, the constraint that σ_e^2 must not be greater than 0.005 is applied, and f_T is set to 0.5. Finally, Figure 28 (32) shows
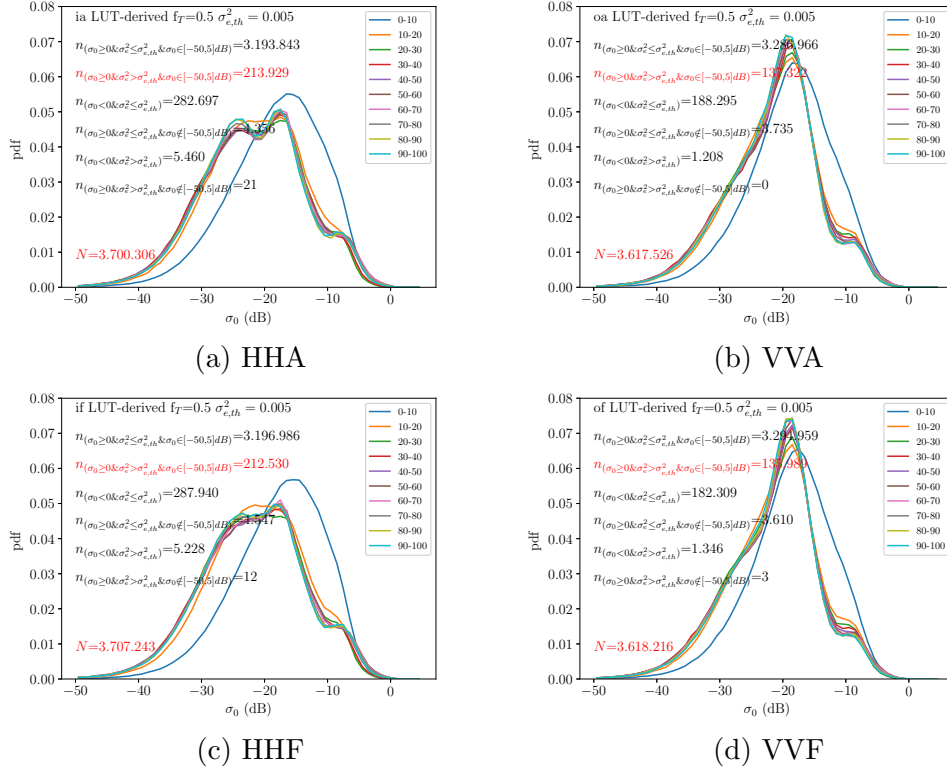
Figure 19: pdf of the slice σ_0s after correction in the interval $[-50, 5]$ dB, segregated according to the distance to the coastline, in a step of 10 km, up to 100 km, when σ_e^{th} is required to be not higher than 0.005. Top-down numbers: a) the number of samples shown; b) the number of positive values that do not match the QC on σ_e^2 in the interval displayed; c) the number of negative values outside the interval that pass the QC; d) the number of positive values that pass the QC but are outside the interval displayed; e) the number of negative values that do not pass the QC; f) the number of positive values that do not pass the QC and are outside the interval displayed. The sum is reported in red at the bottom of the panel.
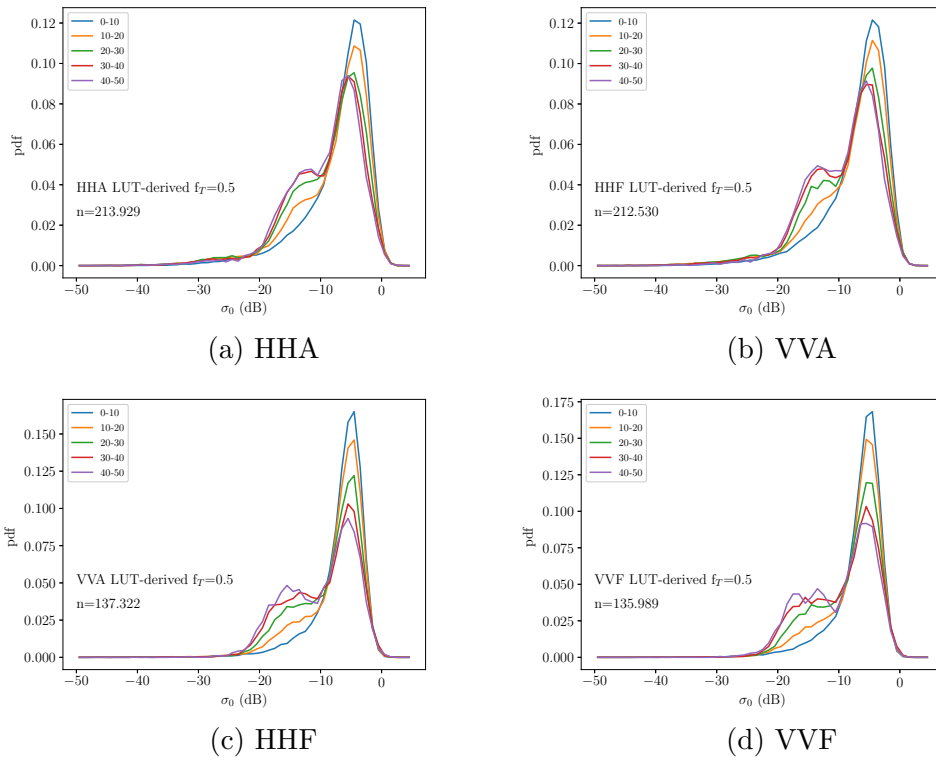
(a) HHA

(b) VVA

(c) HHF

(d) VVF

Figure 20: pdf of the rejected slice σ_0s in the interval $[-50, 5]$ dB, segregated according to the distance to the coastline, in a step of 10 km, up to 100 km, when σ_e^{th} is required to be not higher than 0.005, for each pol-view flavor. The number of samples is indicated in the panels.
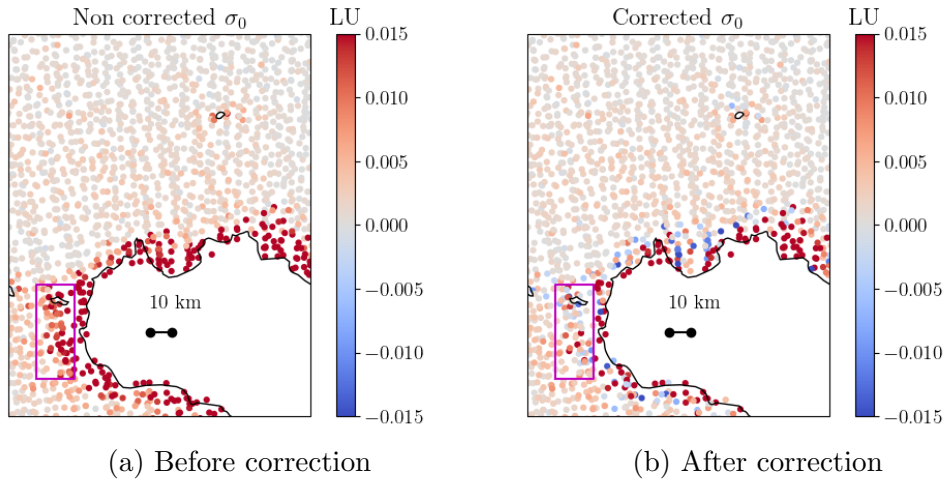
(a) Before correction   (b) After correction

Figure 21: Left (right): σ_0 map offshore Western Sicily before (after) any corrections.

the same plot for Gaussian averaged σ_0s. In the latter case, no constraint on σ_e^2 is applied. As can be seen, coastal sampling improves in general in all these cases, but the analysis carried out in these test areas is not helpful to discriminate among the most performant averaging procedures. In fact, even if coastal sampling improves, some residual contamination appears to occur in all of these methods. In other words, it seems that some additional constraints or tuning are necessary, or an a posteriori QC is needed to filter out the eventually contaminated retrieved winds. Note that here and there some WVCs are missing, especially offshore The Netherlands. In addition to the phenomenon depicted in Figure 24, this may be due to the lack of slice σ_0s with LCR lower than f_T and / or σ_e^2 is greater than 0.005.

Figures 33, 34, 35, 36 show the distributions of the integrated σ_0s of the entire dataset of the 14 orbits dated 10th of April 2007, for each pol-view flavor, segregated according to the distance to the shoreline, when the boxcar, K_p , LCR and Gaussian averaging methods are applied, respectively. The total number of samples is reported in each panel. The differences among the four figures are mainly limited to the blue and orange curves, which represent the distributions of the WVCs closer to the shoreline. This is, of course, expected. Furthermore, note that the larger the distance to the shoreline is, the lower is the difference between the averaging procedure. In fact, in all cases, for open ocean acquisitions, the weights tend to 1, but for K_p-averaging, whose weights depend primarily on SNR. However, such differences do not seem to be that evident. Note that the number of samples is similar for the first three averaging methods mentioned, while it is larger
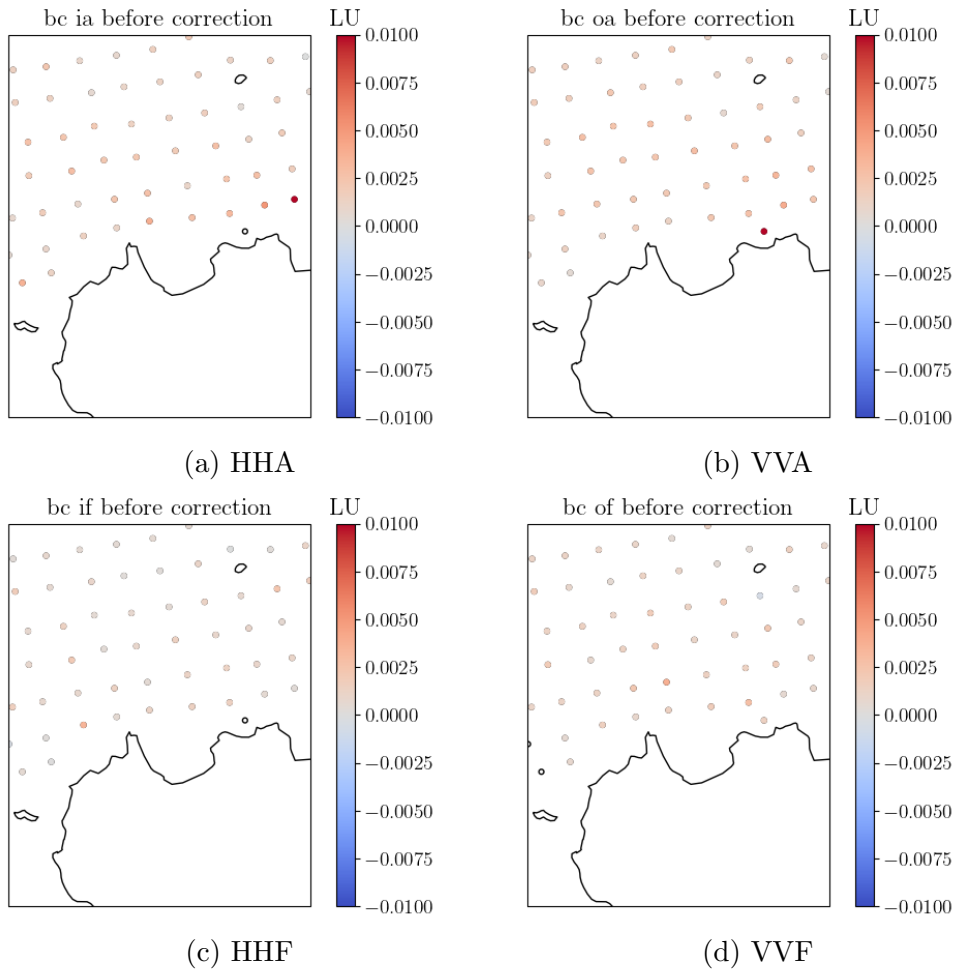
(a) HHA

(b) VVA

(c) HHF

(d) VVF

Figure 22: Integrated σ_0 for each pol-view flavor, before any correction, offshore western Sicily. Slices with LCR higher than 0.02 are excluded, as done for regular open ocean products. The black-framed empty circles represent the WVCs for which the integrated values are missing.
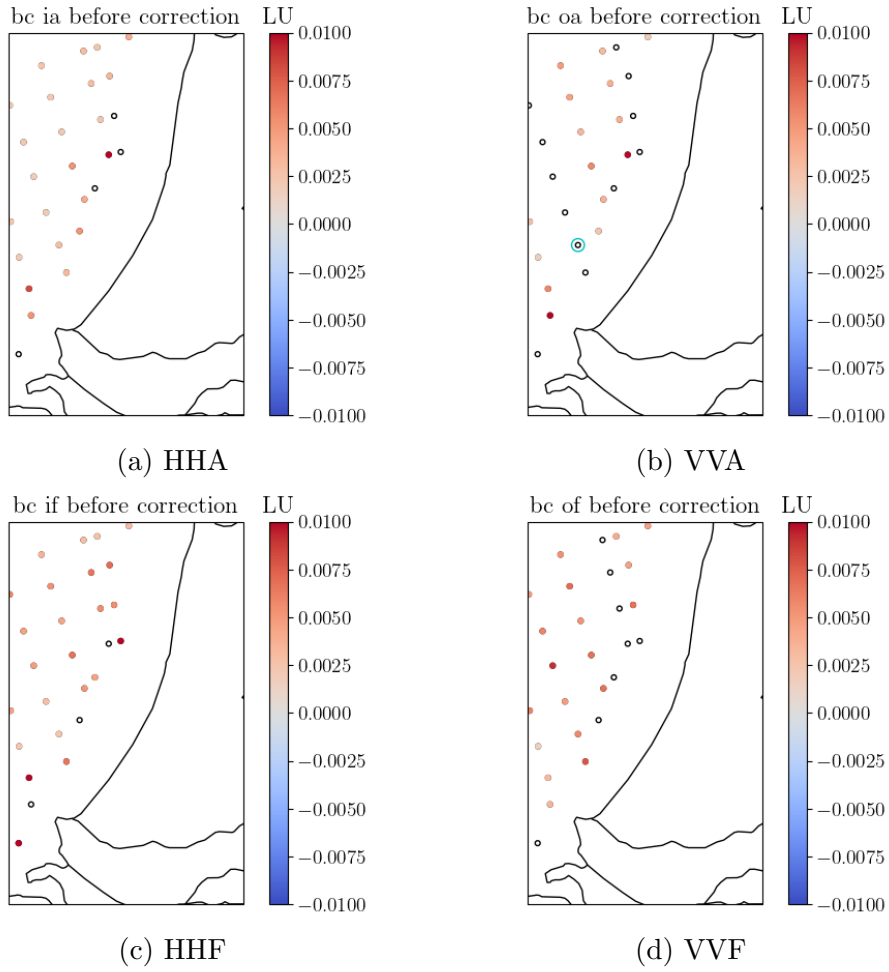
(a) HHA

(b) VVA

(c) HHF

(d) VVF

Figure 23: Integrated σ_0 for each pol-view flavor, before any correction, offshore The Netherlands. Slices with LCR higher than 0.02 are excluded, as done for regular open ocean products. The black-framed empty circles represent the WVCs for which the integrated values are missing.
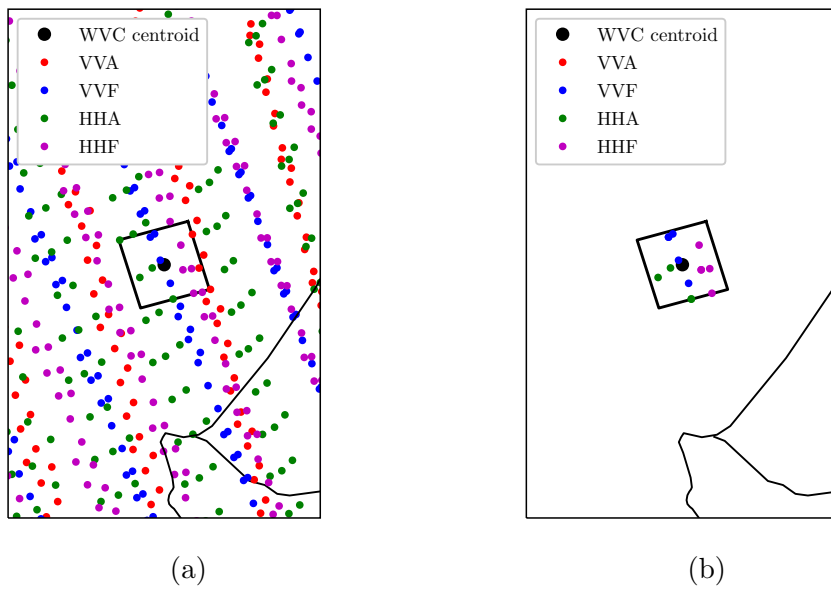
(a)   (b)

Figure 24: Left: slice centroids of all acquisitions off-shore The Netherlands, segregated according to their pol-view flavor. The black circle represents the centroid of the WVC surrounded by a circular cyan frame in Figure 23b, and the black frame represents the entire WVC area before the integration is performed. Right: same as left, but only the centroids of the slices selected for the integration are shown.
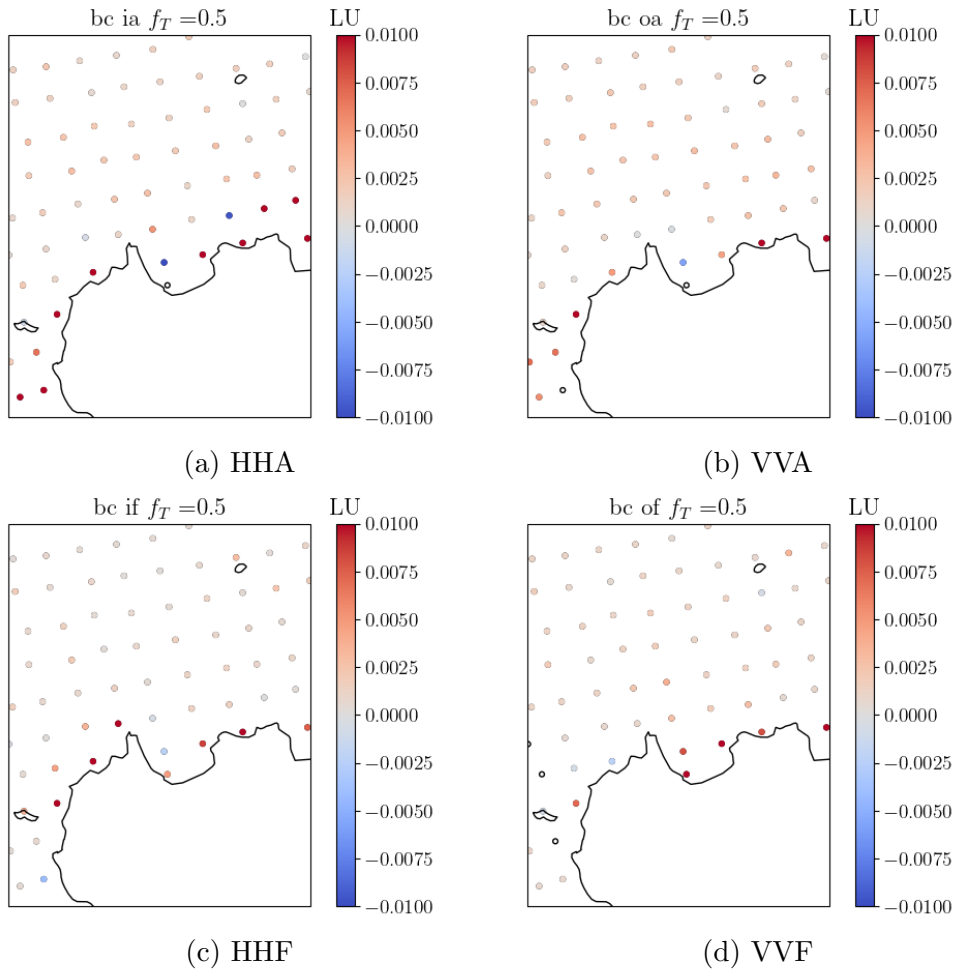
Figure 25: Boxcar averaged σ_0 for each pol-view flavor, offshore western Sicily, after correction with f_T equal to 0.5 and $\sigma_e^2 \leq 0.005$. The black-framed empty circles represent the WVCs for which the integrated values are missing.
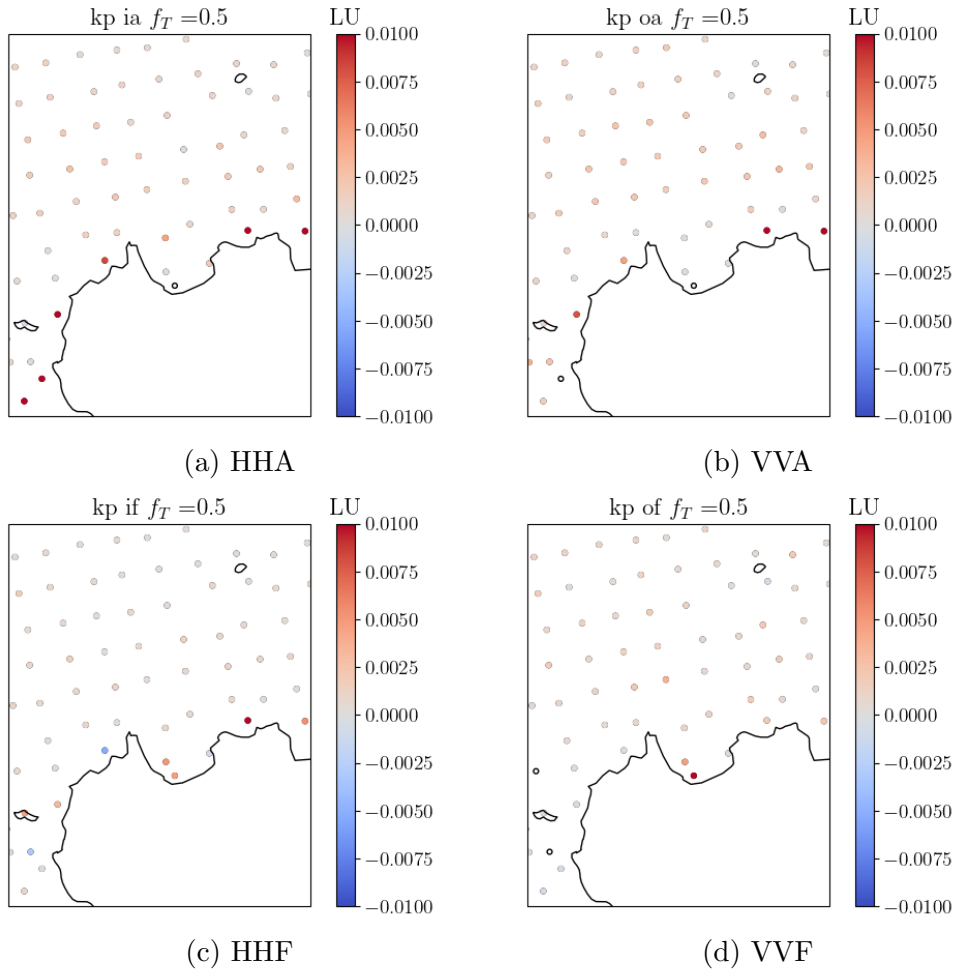
(a) HHA

(b) VVA

(c) HHF

(d) VVF

Figure 26: K_p-averaged σ_0 for each pol-view flavor, offshore western Sicily, after correction with f_T equal to 0.5 and $\sigma_e^2 \leq 0.005$. The black-framed empty circles represent the WVCs for which the integrated values are missing.

Figure 27: LCR-averaged σ_0 for each pol-view flavor, offshore western Sicily, after correction with f_T equal to 0.5 and $\sigma_e^2 \leq 0.005$. The black-framed empty circles represent the WVCs for which the integrated values are missing.
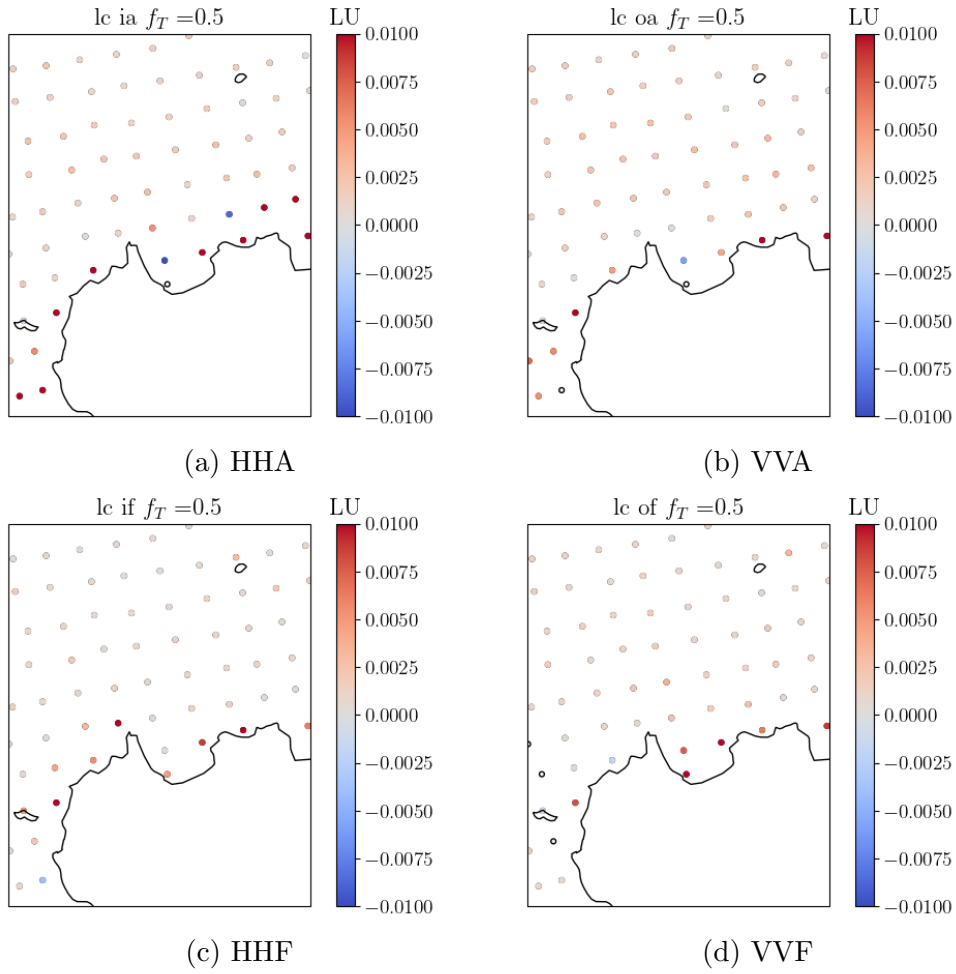
Figure 28: Gaussian-averaged σ_0 for each pol-view flavor, offshore western Sicily, after correction with f_T equal to 0.5. The black-framed empty circles represent the WVCs for which the integrated values are missing.

(a) HHA

(b) VVA

(c) HHF

(d) VVF

Figure 29: Boxcar averaged σ_0 for each pol-view flavor, offshore Netherlands, after correction with f_T equal to 0.5 and $\sigma_e^2 \leq 0.005$. The black-framed empty circles represent the WVCs for which the integrated values are missing.
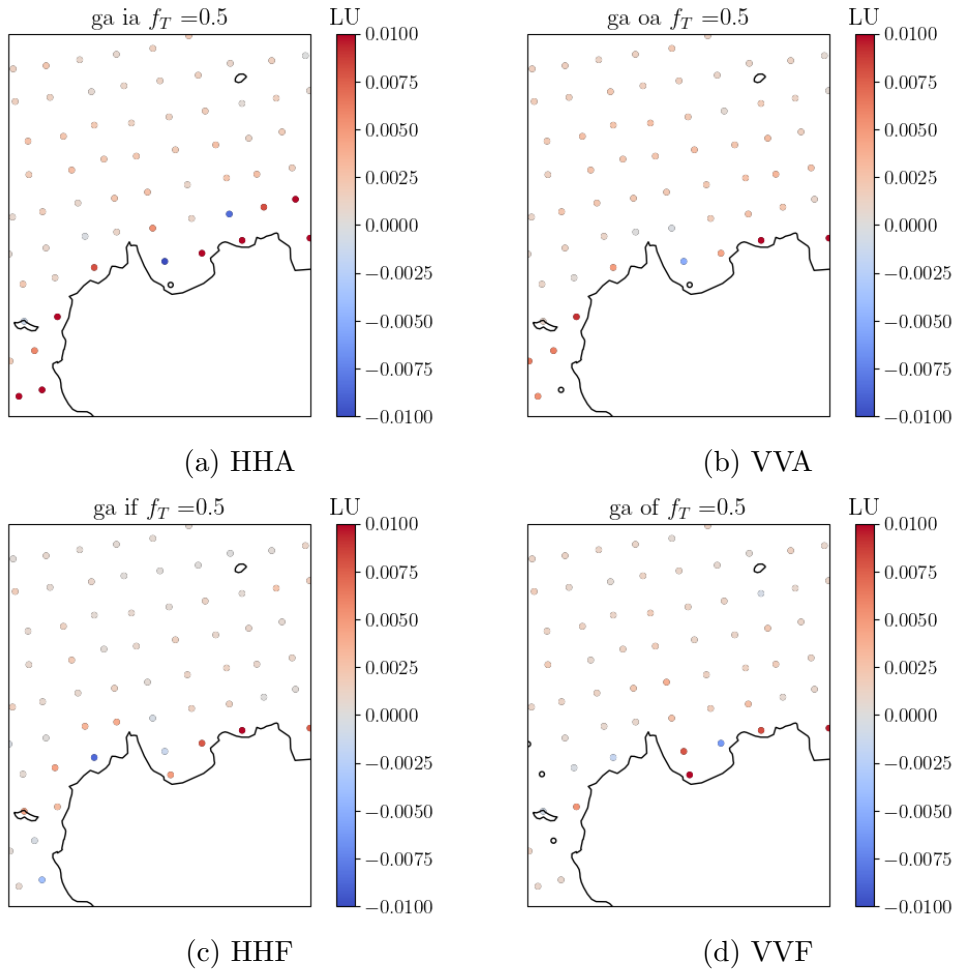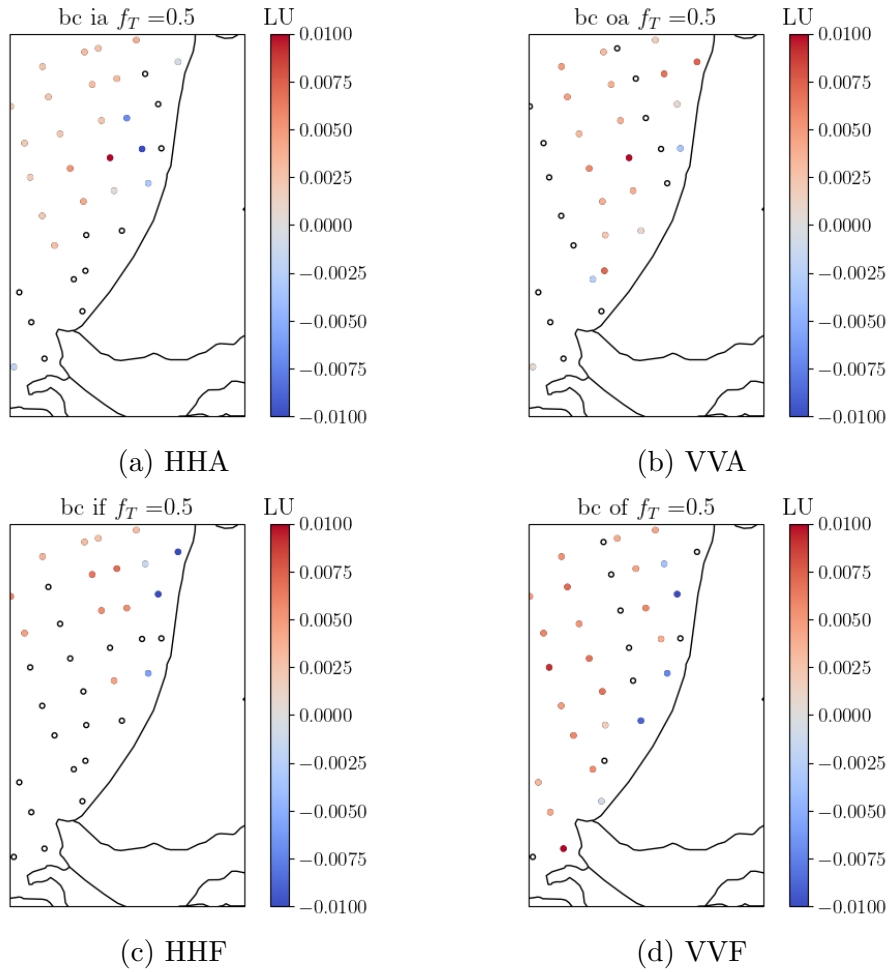
Figure 30: K_p-averaged σ_0 for each pol-view flavor, offshore Netherlands, after correction with f_T equal to 0.5 and $\sigma_e^2 \leq 0.005$. The black-framed empty circles represent the WVCs for which the integrated values are missing.

(a) HHA

(b) VVA

(c) HHF

(d) VVF

Figure 31: LCR-averaged σ_0 for each pol-view flavor, offshore western Sicily, after correction with f_T equal to 0.5 and $\sigma_e^2 \leq 0.005$. The black-framed empty circles represent the WVCs for which the integrated values are missing.
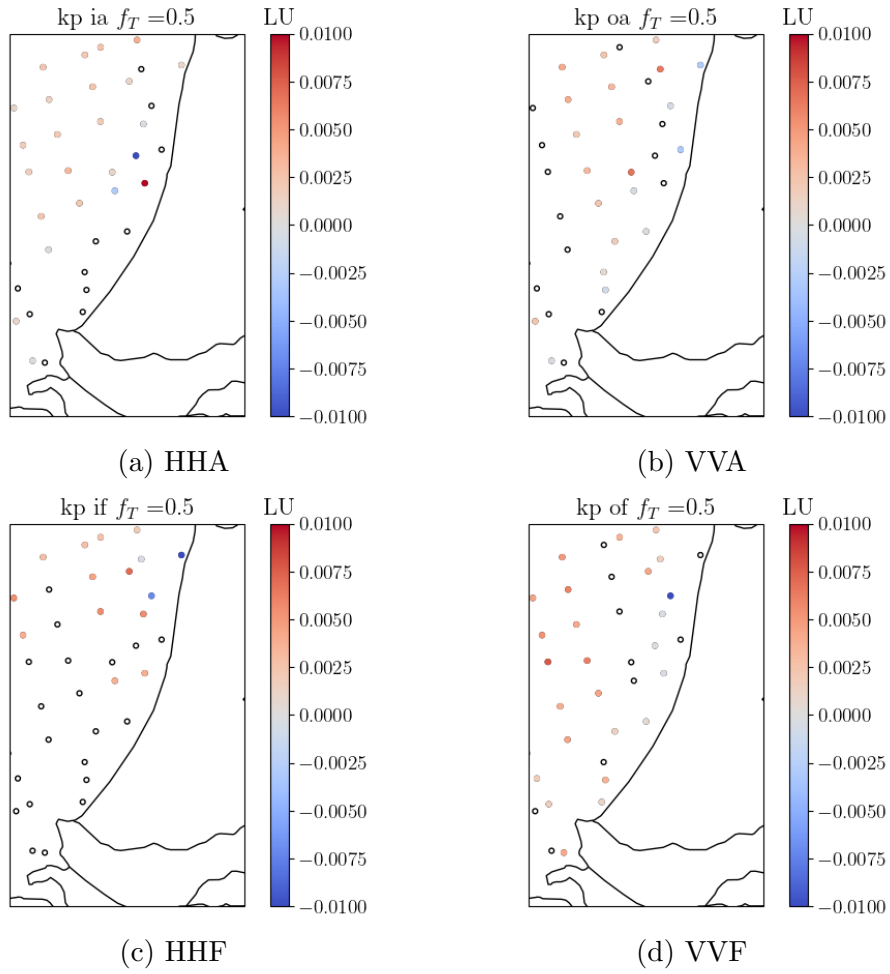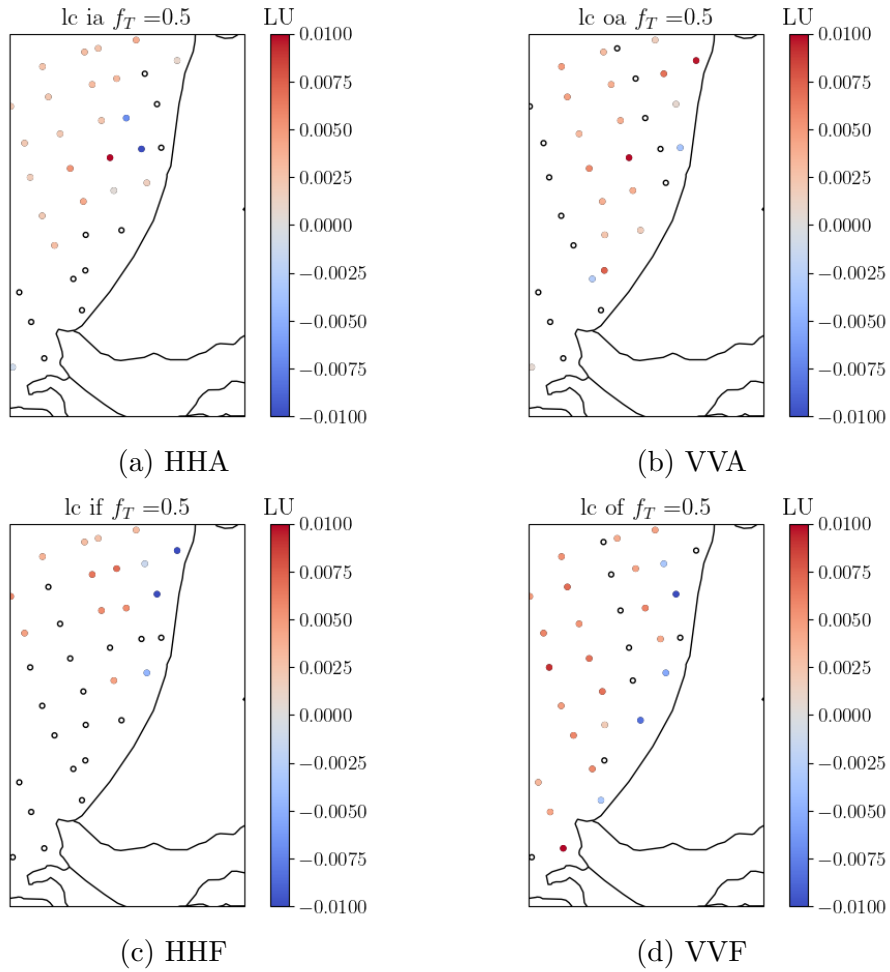
(a) HHA

(b) VVA
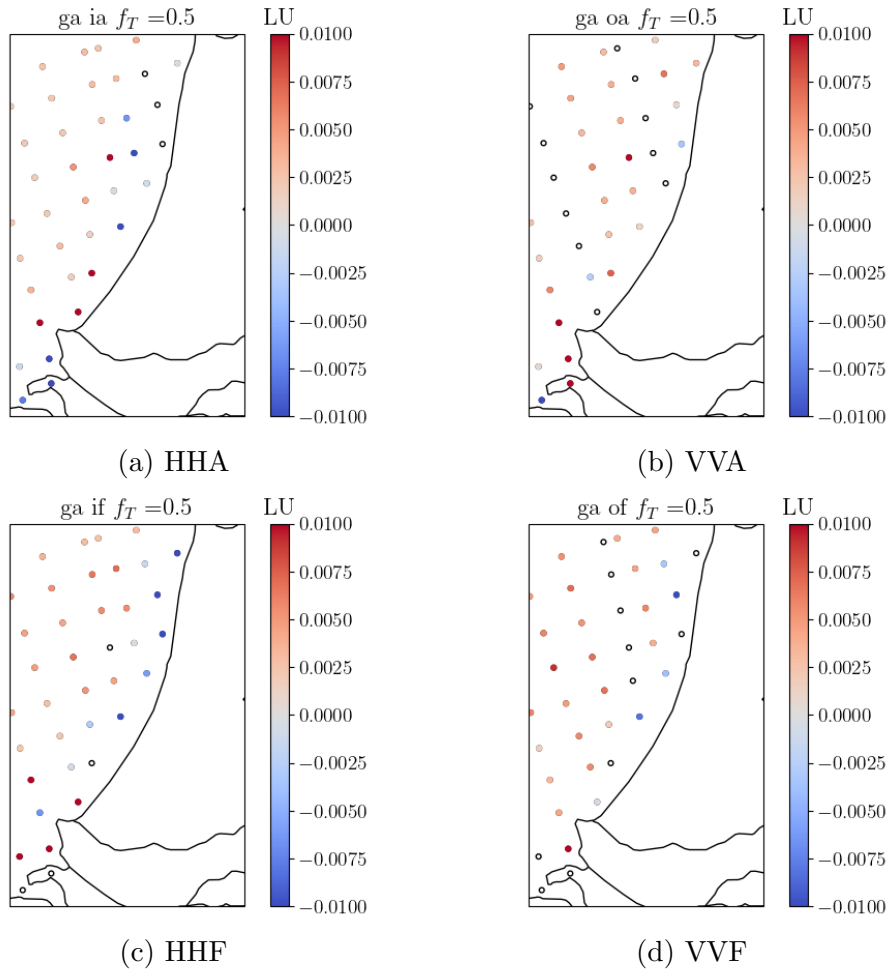
(c) HHF

(d) VVF

Figure 32: Gaussian-averaged σ_0 for each pol-view flavor, offshore Netherlands, after correction with f_T equal to 0.5. The black-framed empty circles represent the WVCs for which the integrated values are missing.
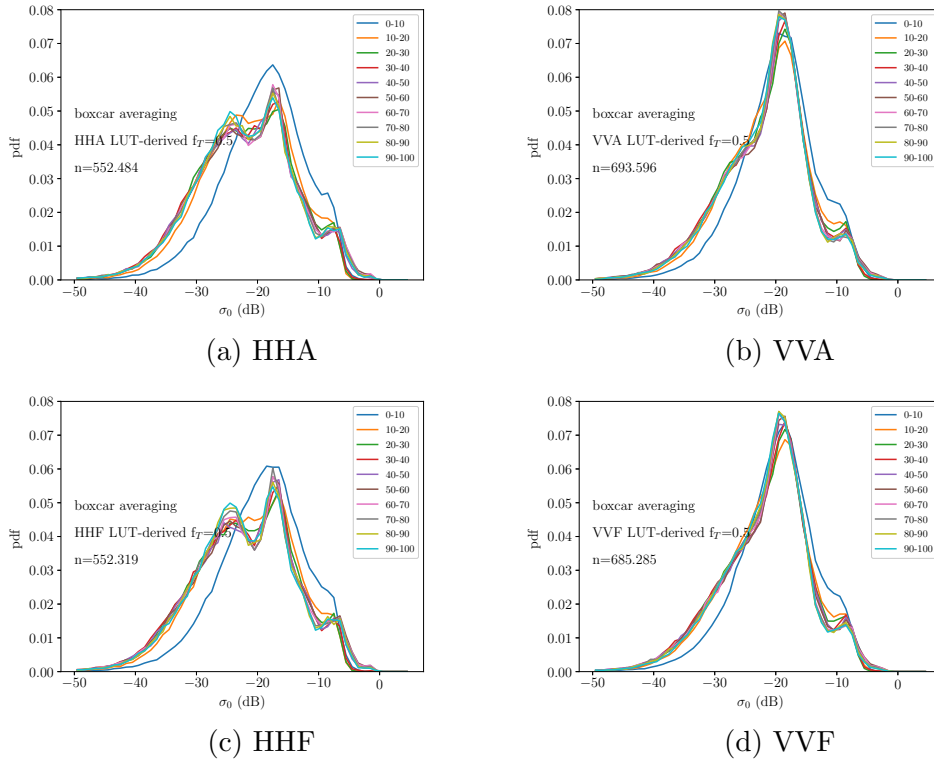
(a) HHA

(b) VVA

(c) HHF

(d) VVF

Figure 33: pdf of the boxcar-averaged σ_0s for each pol-view flavor, segregated according to the distance to the shoreline, when f_T is set to 0.5 and σ_e^2 is not greater than 0.005. The distributions refer to the entire dataset of 14 orbits dated 10th of April 2007 and the total number of samples (WVCs) are reported in the panels.

for Gaussian averaging. In fact, in the latter case, the constraint on σ_e^2 is not applied. Furthermore, for the same reason, the distributions of the Gaussian-averaged σ_0s have some bumps for values ranging from ≈ -5dB to ≈ 0dB, which is more visible for the distributions relating to the WVCs closer to the shoreline (blue and orange curves). These bumps are most likely due to contaminated WVCs, although this cannot be claimed with certainty. This effect could in principle be reduced by tuning the parameter F in the Gaussian averaging formulation. Once more, it seems that much more can be said after the wind field retrieval is performed, and a proper validation is assessed. The blue curves in Figure 34 are closer to the other curves compared to the other averaging procedures. This does not prove that K_p-averaging is the best integration procedure, but should be taken into account in the retrieval step.

(a) HHA

(b) VVA

(c) HHF

(d) VVF

Figure 34: pdf of the K_p-averaged σ_0s for each pol-view flavor, segregated according to the distance to the shoreline, when f_T is set to 0.5 and σ_e^2 is not greater than 0.005. The distributions refer to the entire dataset of 14 orbits dated 10th of April 2007 and the total number of samples (WVCs) are reported in the panels.
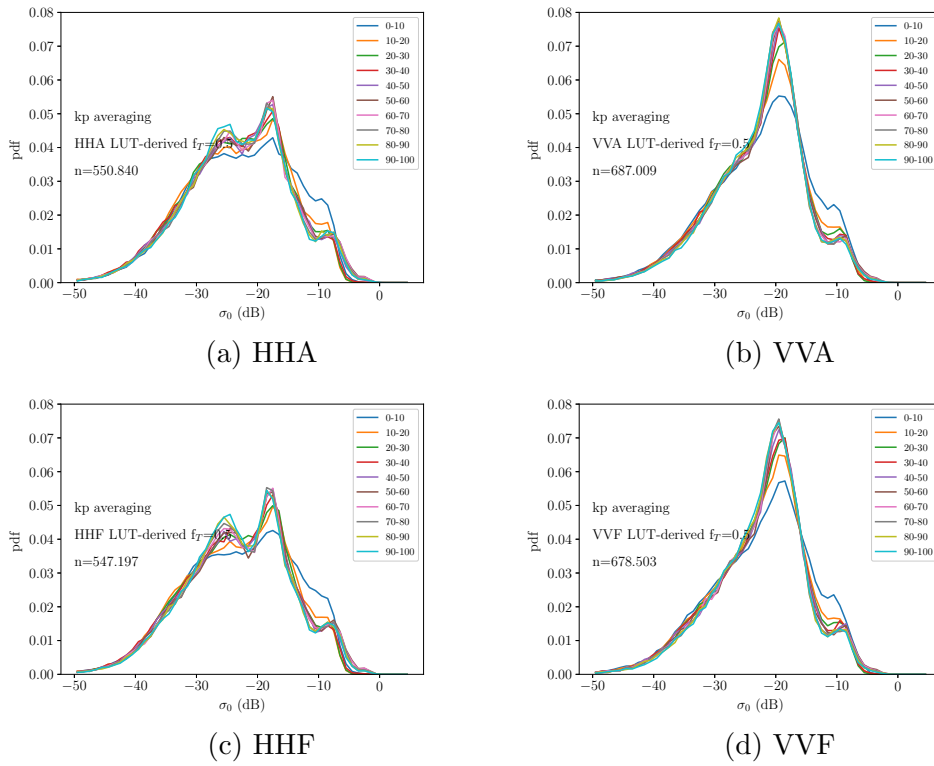
(a) HHA

(b) VVA

(c) HHF

(d) VVF
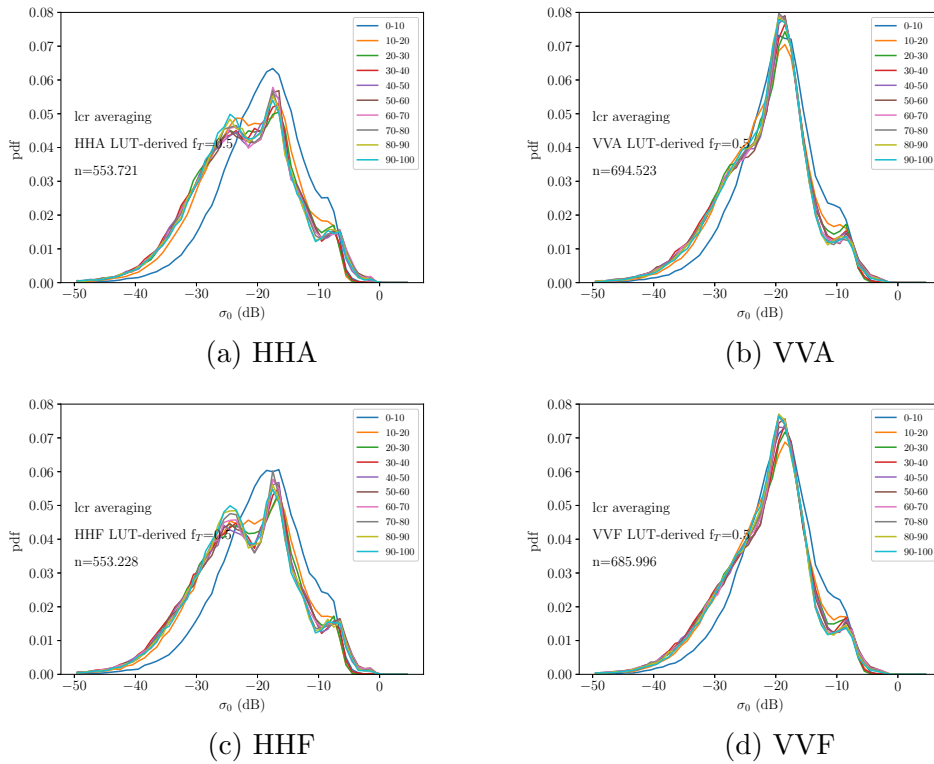
Figure 35: pdf of the LCR-averaged σ_0s for each pol-view flavor, segregated according to the distance to the shoreline, when f_T is set to 0.5 and σ_e^2 is not greater than 0.005. The distributions refer to the entire dataset of 14 orbits dated 10th of April 2007 and the total number of samples (WVCs) are reported in the panels.

(a) HHA

(b) VVA

(c) HHF

(d) VVF

Figure 36: pdf of the Gaussian-averaged σ_0s for each pol-view flavor, segregated according to the distance to the shoreline, when f_T is set to 0.5. The distributions refer to the entire dataset of 14 orbits dated 10th of April 2007 and the total number of samples (WVCs) are reported in the panels.
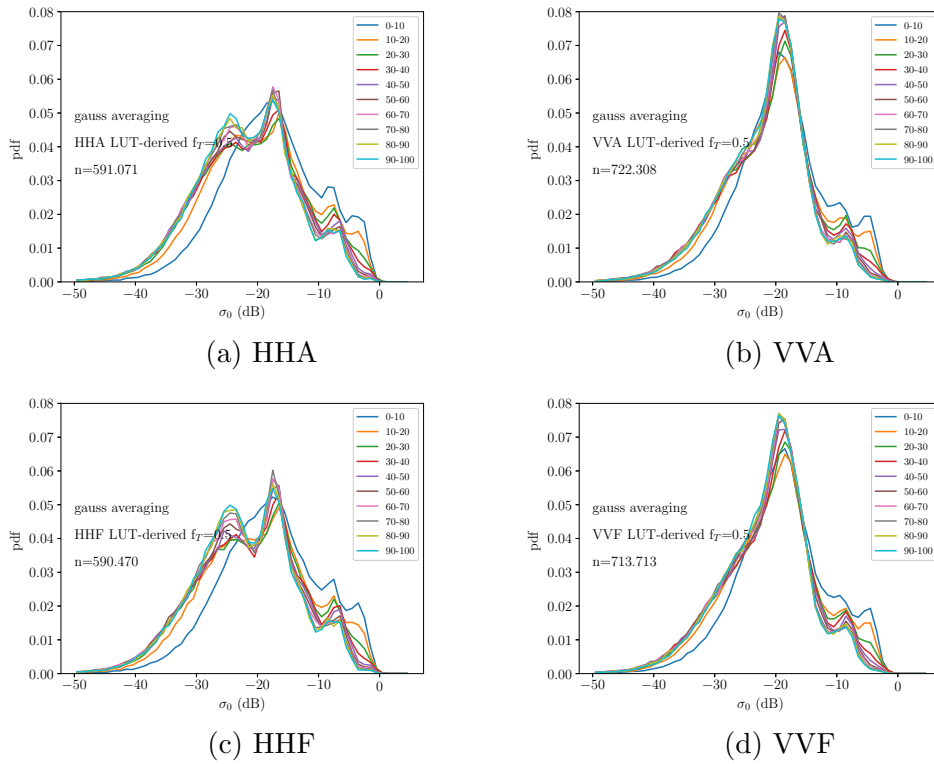
6   Discussion and conclusions

This study presents a refined assessment of the noise that affects the QuikSCAT σ_0 measurements (K_p). Furthermore, it shows the impact of the intra-egg biases induced by the variation of the slice incidence angle on the estimated K_p ($\hat{K}_p$). The methodology applied to estimate $\hat{K}_p$ is identical to that described in [8], but here the assessment is done on a larger dataset, which encompasses all fourteen orbits acquired during the 10th of April 2007. The results show that the new estimates of $\hat{K}_p$ are rather similar to the previous ones, confirming the findings of [8], which are summarized here. There are some significant differences between $\hat{K}_p$ and the median of the values provided in the QuikSCAT full resolution files ($\tilde{K}_p$); in particular, peripheral slices are noisier than declared, especially those with indices 6 and 7, which correspond to those closer to the antenna; on the other hand, central slices seem to be less noisy than declared, especially for V-pol acquisitions; these differences are more notable for medium-high wind regimes. The average biases induced by the deviation of the slice incidence angles w.r.t. the egg centroid are evaluated by means of the GMF NSCAT4DS, and have a rather linear trend w.r.t. the slice index; therefore, they are expected to compensate during the pol-view integration. The worst-case scenario (WCS) biases are evaluated considering the relative wind direction that produces the largest estimated deviations in absolute value, constrained by the sign of the differences. In these cases, the trend of the biases is rather similar, but the values are larger. Even considering the biases in the WCS, the impact on $\hat{K}_p$ is always less than 7% confirming all previous findings.

This study also presents a new method for the computation of LCR [1]. In [8], the LCR was evaluated only considering the contour of -3dB of the SRF (LCR^{-3dB}), while in the new formulation, the entire SRF is considered (LCR^{full}). LCR^{full} seems to give more reliable results when the σ_0 correction scheme is applied.

Finally, this study presents the implementation of the LCR-based σ_0 correction scheme described in [4] for QuikSCAT measurements. The purpose of this method is to eliminate land contamination from coastal acquisitions. This scheme is based on the assumption that the contaminated σ_0 is linearly proportional to LCR. Then the slope (a) and the offset (b) of this linear curve are fitted and used to estimate σ_0^{SEA}. The correction is only applied to σ_0s with LCR lower than f_T. In this study, two values of f_T are considered: 0.2 and 0.5. The distributions of a, b and the regression error (σ_e^2) do not suggest any threshold value for QC, in line with the findings of [4]. The distributions of the slice σ_0s are analyzed before and after correction, together with their maps, in two area tests: offshore The Netherlands and offshore western Sicily,

in the Mediterranean basin. The visual comparison of σ_0s in the two area tests suggests that the correction is effective in reducing the values. This is in line with expectations, as land contamination generally increases σ_0. However, the number of negative σ_0s largely increases after correction, up to $\approx 250\%$ more in the 50 km strip closer to the shoreline. Actually, this trend is expected, since QuikSCAT acquisitions are very noisy. In addition, the linear regression applied in this scheme is based on two fundamental hypotheses: a) σ_0^{LAND} is homogeneous in the area of interest; b) the level of noise does not depend on LCR. Both may be too strong. In particular, the higher the LCR is, the higher is the land contamination, and, in general, so is σ_0.

Distributions before and after correction are segregated according to the distance to the shoreline, in steps of 10 km to 100 km. Their comparison shows that corrections mainly impact the acquisitions with 20 km to the shoreline, as expected. When a threshold value of 0.005 is used for σ_e^2, the impact on the distributions is more visible. Most rejected values are within -10 and -5 dB, as expected. However, this threshold value is arbitrary since, as said above, the distribution of σ_e^2 does not suggest any threshold value. Gaussian averaging can overcome the problem of finding a suitable threshold value for σ_e^2, but some a posteriori QC is needed after retrieval.

Integration of the slice σ_0s into σ_0^{pv} gives different results, according to the averaging method chosen, even if some residual land contamination seems to be common to all. Fine-tuning of the Gaussian weights may help to reduce such contaminations. The results in the two area tests suggest that in some areas a WVC grid spacing of 12.5 km could be excessively fine and that a lack of slice σ_0s is likely to occur. Preliminary results are not sufficient to select the most suitable averaging methodology; therefore, the retrieval step is necessary for this purpose.

7 Future work

The preliminary results of this study suggest that additional steps are still needed on both the scientific and software development sides. The implemented LCR-based σ_0 correction scheme proves to be effective in reducing land contamination, but too many negative values result. The reason is likely due to the high level of noise that affects QuikSCAT measurements, which increases with the value of σ_0. Therefore, the correction values estimated by linear regression should be scaled with an additional noise-dependent regularization parameter, as depicted in Equation 7.1.

$$\sigma_0^{SEA} = \alpha(\sigma_0 - af - b) + b \qquad (7.1)$$
$$\alpha = \frac{\sigma_{\bar{\sigma}_0^{SEA}}}{\sigma_{\bar{\sigma}_0^f}}$$

where $\sigma_{\bar{\sigma}_0^{SEA}}$ represents the noise level for the sea and $\sigma_{\bar{\sigma}_0^f}$ represents the noise level for the contaminated σ_0, and $\bar{\sigma}_0^{SEA}$ and $\bar{\sigma}_0^f$ are the values of the regression curve in LCR equal to 0 (b) and f, respectively. In [8], it has been shown that the level of noise is rather similar for sea and all kinds of surfaces. This means that the level of noise strictly depends on the level of σ_0. If one knows the expected K_p for a wide range of σ_0 levels, α can easily be estimated. α is expected to be between 0 and 1, decreasing with f; therefore, it should decrease the absolute value of the correction and maintain its sign. In fact, even if $\hat{K}_p$ has been shown to decrease with the level of σ_0, σ_{σ_0} increases with σ_0, since K_p is a noise-to-signal ratio by definition. The methodology described in this study for the estimation of $\hat{K}_p$ can be used to evaluate a look-up table of K_p throughout the entire range of expected σ_0s. Both methods must be validated after the retrieval step is performed.

The software is mature enough to be embedded in `PenWP` and / or implemented in a more efficient low-level programming language, such as FORTRAN or C. The most time-consuming part of the code is related to the computation of the LCR, for which an optimization is urgent. The tool `seawinds_l1b_bufr` must be updated to transform full resolution files into suitable bufr files at 12.5 km WVC spacing to be fed in `PenWP`; in addition, it must be purged of some bugs, such as the one related to the association of the slice centroids with the WVCs. At the moment, `PenWP` can only handle 25 km WVC grids; therefore, it must be updated to handle 12.5 km WVC grids.

References

[1] M. P. Owen and D. G. Long, "Land-contamination compensation for quikscat near-coastal wind retrieval," *IEEE Transactions on Geoscience and Remote Sensing*, vol. 47, no. 3, pp. 839–850, 2009.

[2] R. D. Lindsley, J. R. Blodgett, and D. G. Long, "Analysis and validation of high-resolution wind from ascat," *IEEE Transactions on Geoscience and Remote Sensing*, vol. 54, no. 10, pp. 5699–5711, 2016.

[3] R. D. Lindsley, C. Anderson, J. Figa-Saldaña, and D. G. Long, "A parameterized ascat measurement spatial response function," *IEEE Transactions on Geoscience and Remote Sensing*, vol. 54, no. 8, pp. 4570–4579, 2016.

[4] J. Vogelzang and A. Stoffelen, "Ascat land correction, report for the eumetsat ocean and sea ice saf," tech. rep., Koninklijk Nederlands Meteorologisch Instituut, 2022. SAF/OSI/CDOP3/KNMI/TEC/TN/384.

[5] G. Grieco, M. Portabella, J. Vogelzang, V. A., and S. A., "Initial development of pencil-beam scatterometer coastal processing," tech. rep., Barcelona Expert Center (BEC ICM-CSIC), 2020. OSI-SAF VS Technical Report # OSI-SAF 20-01.

[6] A. Tarantola, *Inverse Problem Theory and Methods for Model Parameter Estimation*. Society for Industrial and Applied Mathematics, 2005.

[7] C. Anderson, H. Bonekamp, C. Duff, J. Figa-Saldana, and J. J. W. Wilson, "Analysis of ascat ocean backscatter measurement noise," *IEEE Transactions on Geoscience and Remote Sensing*, vol. 50, no. 7, pp. 2449–2457, 2012.

[8] G. Grieco, M. Portabella, J. Vogelzang, V. A., and S. A., "Quikscat normalized radar cross section noise characterization for coastal wind field retrieval," tech. rep., Istituto di Scienze Marine (ISMAR-CNR), 2021. OSI-SAF VS Technical Report # OSI-SAF 20-03.

[9] R. E. Fischer, "Standard deviation of scatterometer measurements from space," *IEEE Transactions on Geoscience Electronics*, vol. 10, no. 2, pp. 106–113, 1972.

[10] "https://podaac-opendap.jpl.nasa.gov/opendap/."

[11] Thorlabs, *QuikSCAT Science Data Product. User's Manual.* JPL NASA.